scientific reports

OPEN

Unsegmented marine annelids as biomechanical models for soft robotics

Linda Paternò[1,5], Joachim Langeneck[2,5], Kleoniki Keklikoglou[3], Ilaria Cedrola[1], Alessandra Martines[2,4], Mohammad Hasan Dad Ansari[1], Desirèe Dimichele[2,4], Emmanouela Vernadou[3], Jacopo Quaglierini[1], Antonio De Simone[1,6], Luigi Musco[2,4,6] & Arianna Menciassi[1,6]✉

This work investigates marine worms as a source of bioinspiration for soft robotics, focusing on *Phascolosoma stephensoni* (Annelida), an unsegmented sipunculan species with a fully eversible introvert capable of remarkable elongations. High-resolution micro-computed tomography was used to resolve the internal musculoskeletal architecture across functional configurations. Morphometric analyses of live specimens revealed strong differentiation between body regions: trunk length remains nearly constant during motion (7.26 ± 3.40 mm retracted vs. 7.70 ± 3.47 mm extended), whereas total body length more than doubles (from 8.87 ± 4.30 mm to 18.75 ± 7.35 mm), driven by introvert eversion at the tip. Tensile tests further highlighted distinct mechanical properties, with the trunk sustaining substantially higher strains before failure (≈ 90–110%) compared to the introvert (≈ 60–65%). Peristaltic locomotion was investigated using a mathematical model reproducing wave-like propulsion in unsegmented bodies at characteristic speeds of 0.5–5 mm s^{-1} in confined media and showing close agreement with experimental observations. As an exemplary translation of these mechanisms, a soft robotic architecture based on magneto-responsive silicone was developed enabling stimulus-driven protrusions up to 2.5 times the initial length. Overall, this study provides a biologically grounded framework for innovative soft robotic systems inspired by unsegmented worms.

Keywords Bioinspired robotics, Marine worms, Soft robotics, Worm kinematics, Physical intelligence

In nature, many soft-bodied organisms demonstrate how shape change and force transmission can emerge through continuous deformation rather than articulated motion, employing hydrostatic skeletons as a remarkably effective strategy for movement, structural support, and the dynamic control of form and force[1,2]. In soft robotics, these biological architectures provide a compelling natural blueprint, illustrating how the coordinated arrangement of muscle layers, internal pressure, and anisotropic reinforcement enables soft bodies to modulate stiffness, speed, and mechanical advantage, dynamically reconfiguring their structure to meet changing functional demands[1,3].

Among the diversity of living organisms, worms stand out as an especially rich source of bio-inspiration. Their movement and shape changes emerge from the coupling between body mechanics and continuous interaction with the environment, enabling constant adaptation while embedding part of their behavioral control within the body's morphology and material properties[4,5]. This form of physical intelligence[6] makes worms ideal biological models for the development of autonomous soft robotic systems capable of overcoming traditional centralized control by exploiting interactions with their surroundings through soft shape-morphing architectures and stimuli-responsive materials[5].

Most previous bio-inspired designs inspired by worms have focused on the cooperation of independent modular units, drawing clear inspiration from the metameric organization of segmented Annelida such as oligochaetes and polychaetes[7–9]. In contrast, unsegmented annelids remain largely unexplored, even though

[1]The BioRobotics Institute, and Department of Excellence in Robotics & AI, Sant'Anna School of Advanced Studies, Pisa, Italy. [2]National Interuniversity Consortium for Marine Sciences (CoNISMa), Rome, Italy. [3]Institute of Marine Biology, Biotechnology and Aquaculture (IMBBC), Hellenic Centre for Marine Research (HCMR), Heraklion, Crete, Greece. [4]Department of Biological and Environmental Sciences and Technologies (DiSTeBA), University of Salento, Lecce, Italy. [5]These authors contributed equally to this work: Linda Paternò and Joachim Langeneck. [6]These authors contributed equally to this work: Luigi Musco, Arianna Menciassi and Antonio De Simone. ✉email: arianna.menciassi@santannapisa.it

these worms are capable not only of performing traditional peristaltic locomotion but also of producing large protrusions through the eversion of proboscis-like body structures. Among them, Sipuncula are particularly noteworthy due to their structural simple yet mechanically efficient body architecture, capable of both peristaltic movement and body elongations exceeding 200% of their resting length[10]. Once considered a separate phylum, these worms were later recognized as one of the earliest lineages to diverge from the annelids, as evidenced by Cambrian fossils and molecular phylogenies[11–13]. Even though recent studies strongly support the hypothesis of Sipuncula being part of the annelid radiation, the precise phylogenetic position of this group is still object of some debate. Additionally, the systematics of Sipuncula, traditionally based on internal anatomy, and in particular on the number and position of retractor muscles, turned out to be largely inconsistent with the phylogeny of the group[14,15]. Lastly, several species are currently considered cosmopolitan, in contrast with the biogeographical patterns typically retrieved in marine invertebrates, possibly as a consequence of their extremely simple anatomy and low number of diagnostic characters[16]. It appears evident that the diversity, evolution and ecology of this group is still in need of detailed studies. Unlike other unsegmented annelids, sipunculids show no trace of segmentation at any life stage and lack chaetae, circulatory vessels, and respiratory pigments. In these organisms, a single continuous, fluid-filled coelomic cavity (representing the hydrostatic skeleton) spans the entire body, enabling deformations that involve the whole organism. Sipuncula are characterized by the presence of a fully eversible introvert, the protrusion of which is driven by compression of the coelomic fluid by a layer of circular muscles, while the retraction is due to the action of two or four retractor muscles typically inserted in the posterior part of the body and extending across the coelomic cavity to the tip of the introvert[17]. Unsegmented sipunculans can therefore be regarded as simplified biomechanical models from which design principles of fully continuum hydrostatic architectures may be derived, providing a conceptual alternative to the predominantly modular paradigm in worm-inspired robotics. A continuous, non-segmented organization enables uniform pressure propagation within a single coelomic cavity, resulting in smoother and more evenly distributed force transmission; it minimizes interfacial stress concentrations associated with discrete modules, thereby improving structural robustness; reduces fabrication complexity and facilitates scalability and miniaturization by eliminating the need for multiple chambers, valves, or rigid connectors; promotes spatially continuous deformation rather than stepwise motion; and enhances adaptability to irregular or unstructured environments. Together, these features broaden the architectural design space of bioinspired soft robotic systems.

The protrusion mechanism of Sipuncula has served as a model for the design of systems such as vine robots[18,19], in which a flexible plastic tube everts through internal pressurization, producing tip extension that mimics growth. Another solution mimicked the action of circular muscles by enclosing a fluid-filled passive chamber within a braided mesh inside a cylindrical pneumatic actuator, whose radial compression induces longitudinal elongation of the passive chamber, reproducing the circumferential–axial coupling observed in Sipuncula[20]. Like most worm-inspired soft robots, both mentioned designs rely on pneumatic actuation, lacking the physical intelligence of real worms whose compliant bodies adaptively react to their surroundings. In this regard, soft stimuli-responsive materials open new possibilities by providing alternative actuation strategies that inherently couple sensing, actuation, and control within the material itself[21]. In this regard, soft materials embedded with hard magnetic particles can be programmed with specific magnetization profiles that enable controlled dynamic shape morphing under wireless and safe external magnetic fields[22–24]. By emulating the natural responsiveness of worms to environmental cues, this approach would allow soft robots to exhibit reactive behaviors that better reproduce the adaptive capabilities of biological worms, while at the same time enabling a broad spectrum of applications that demand compact, safe, and remotely controlled actuation. For instance, Lin et al.[25] developed a magnetic-driven folded diaphragm inspired by the segmented structure of earthworms. Thanks to radial magnetization, the diaphragm can transform from a flat to an unfolded configuration under a uniform magnetic field, reaching displacements of about 5 mm for prototypes with a diameter of ~ 20 mm.

In this work, focusing on the sipunculan species *Phascolosoma stephensoni* (Stephen, 1942), we systematically analyzed its anatomy and morphology through an integrated morphometric and biomechanical investigation. This analysis encompassed peristaltic locomotion, introvert protrusion, and the mechanical properties of soft tissues, providing a comprehensive characterization of the organism's hydrostatic-driven deformation and movement strategies. By quantitatively linking structure, mechanics, and function, this study elucidates how effective locomotion and large shape changes can emerge in a continuous, unsegmented body. Building on insights gained from the musculoskeletal organization and biomechanical performance of *P. stephensoni*, we also developed a soft robotic prototype based on magneto-responsive composites, specifically designed to replicate the hydrostatic-driven protrusion of the introvert observed in the biological model. This prototype serves as an illustrative translation of the identified biological principles into an engineered system, demonstrating the relevance of the analyses for the design of novel soft robotic architectures inspired by unsegmented organisms.

Results

Anatomy and morphology

As observed in other sipunculan species, *P. stephensoni* exhibits a bilaterally symmetric, unsegmented body that can be divided into two main functional regions along the anterior–posterior axis: the introvert and the trunk (Fig. 1).

The introvert is a proboscis-like, fully eversible anterior body region that functions in both feeding and locomotion. It is equipped with numerous papillae and, near the distal end of the introvert, cuticular hooks or spines arranged in transverse rows. These structures aid in anchoring and burrowing and show variability among individuals and developmental stages. At the tip of the introvert is located the mouth, typically surrounded by a small number of tentacles representing sensory structures or perioral lobes used for deposit feeding. The mouth leads to a pharynx and a long, coiled gut that runs through the trunk. Unlike segmented annelids, *P. stephensoni* lacks external or internal segmentation, and completely lacks chaetae; cuticular hooks are the only

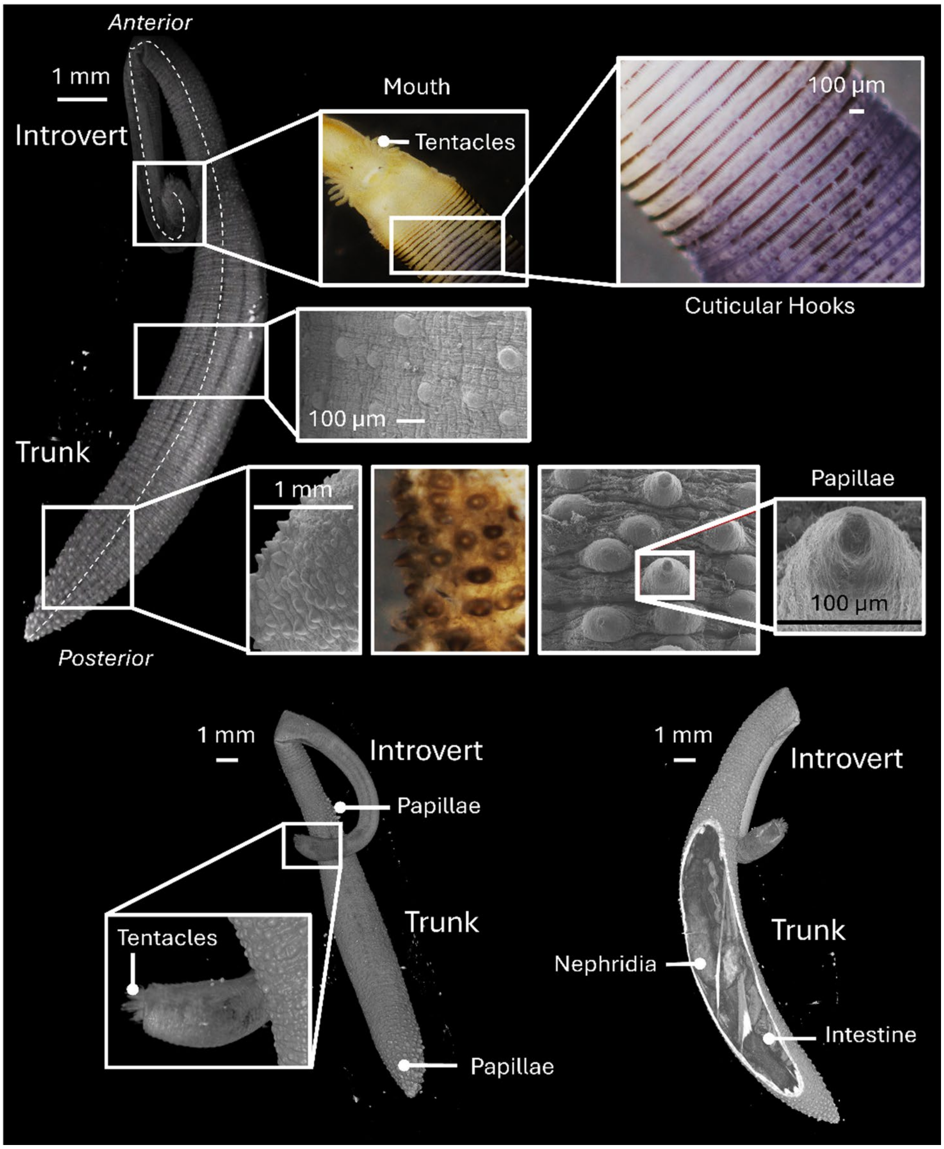

Fig. 1. Micro-computed tomography (micro-CT) scans of *P. stephensoni*, together with scanning electron microscopy (SEM) and digital optical microscopy (Hirox) images, showing external and internal anatomical features. External views illustrate the mouth surrounded by tentacles, the cuticle with hooks on the introvert, and papillary protrusions on the trunk (sparser along the body and denser toward the distal end). Internal micro-CT reconstructions reveal the organization of the coelomic cavity and major internal structures, including the nephridia, and intestine.

hard structure and are collagen-based rather than chitinous. The trunk is a thicker, cylindrical region that houses most internal organs, including the digestive tract, nephridia, gonads, and a spacious coelomic cavity filled with fluid. This cavity acts as a hydrostatic skeleton and plays a crucial role in body extension mechanics.

The trunk wall is composed of an outer cuticle, an epidermal layer, and two main muscle layers: an outer circular and an inner longitudinal musculature (Fig. 2). The longitudinal musculature is composed of several longitudinal, parallel traits (particularly evident in the retracted position), which can be activated independently from each other, allowing for the bending through differential contraction. Anatomically, the sipunculan body, composed of trunk and introvert, can be modeled as a closed, two-compartment hydrostatic system with constant total volume, similar in principle to the tube foot mechanism described by Ellers et al.[1] for echinoderms. A key distinction is that, in sipunculans, the introvert is fully enclosed within the trunk when retracted, and only a basal region -through which it attaches to the trunk-remains external even in the retracted configuration (Fig. 3; Table 1). This basal portion represents a gradual transition zone that is more rugose and progressively tapers. When the circular muscles of the trunk contract and the retractor muscles relax, the radius of the trunk is reduced, and the coelomic fluid within the coelomic cavity of the hydrostatic skeleton is compressed. According to Pascal's principle, this compression raises internal pressure, generating a pushing force and a volume displacement from the trunk into the introvert, promoting its eversion and elongation. Since the fluid volume

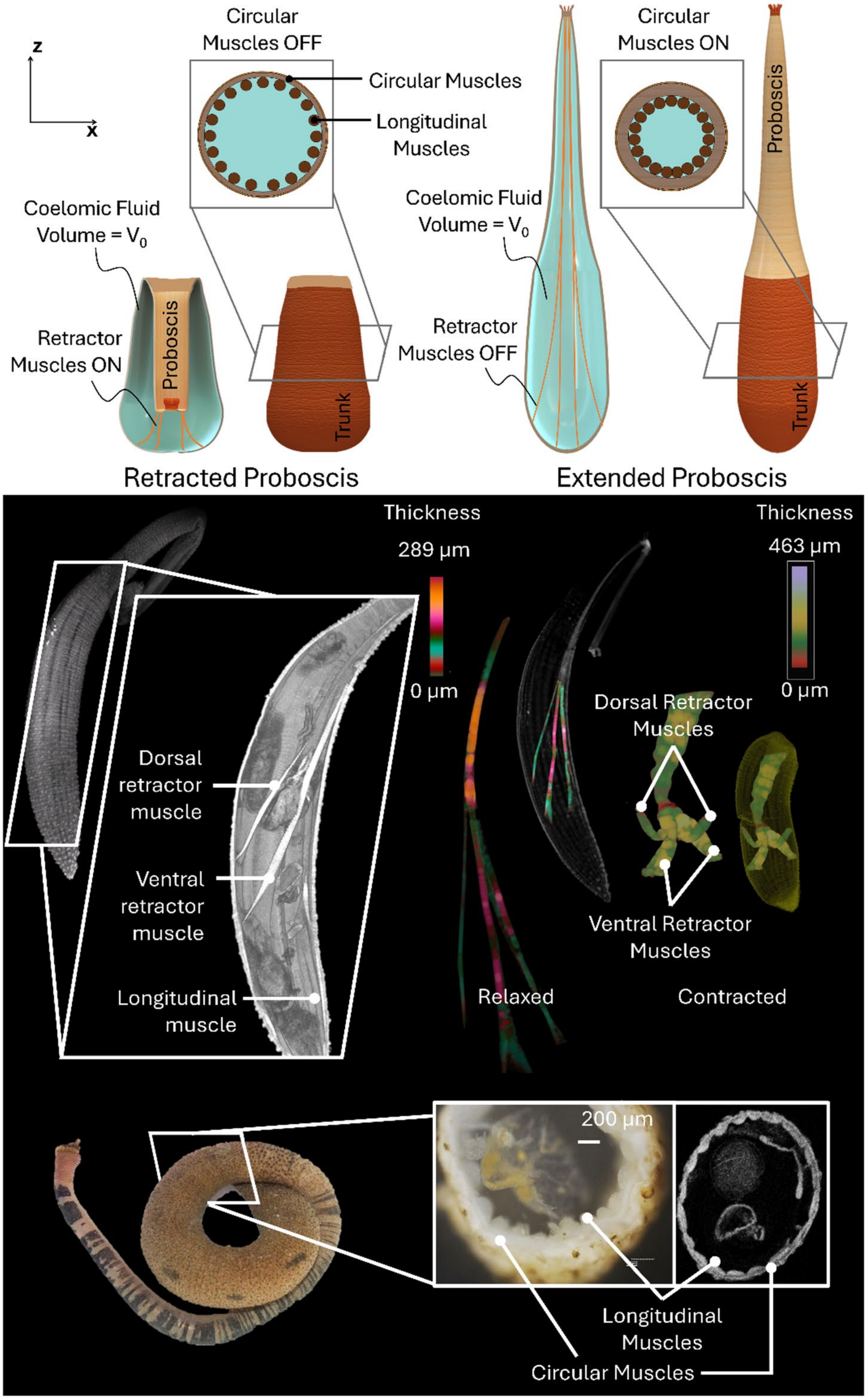

Fig. 2. Top: Schematic of the musculoskeletal structure of *P. stephensoni* illustrating the mechanism of introvert protrusion. Starting from a configuration in which the introvert is retracted into the trunk due to the contraction of the retractor muscles (left), it is then protruded outward by the contraction of the trunk's circular muscles and the constant volume of the coelomic fluid within the hydrostatic skeleton (right). Middle: micro-computed tomography (micro-CT) scans of the worm showing the retractor muscles in their relaxed (elongated and thinner) and retracted (shortened and thicker) states. The colormap indicates muscle thickness in the two configurations. Bottom: digital optical microscopy (Hirox) and micro-CT images showing the arrangement of longitudinal and circular muscles in the body wall.

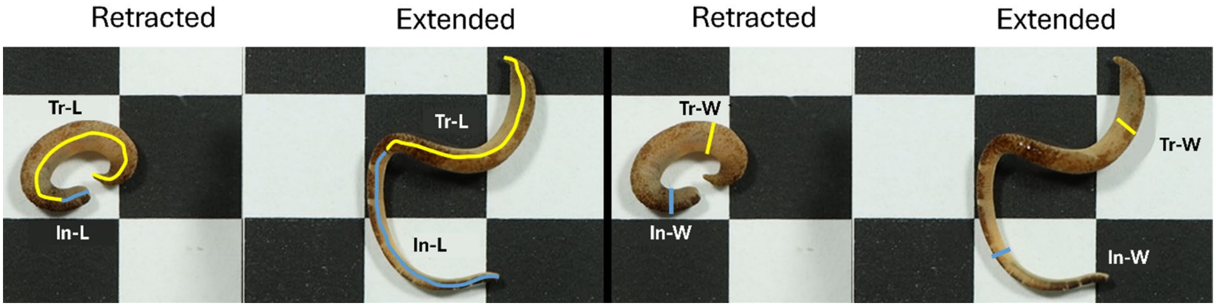

Fig. 3. Frames showing the fully retracted and fully extended states of *P. stephensoni*, extracted from high-resolution video recordings. Yellow lines indicate trunk measurements, and blue lines indicate introvert measurements, highlighting the morphological changes between retracted and extended states. Lengths were measured along the curvilinear longitudinal axis of each body region, whereas widths were recorded at the midpoint of the trunk and introvert, perpendicular to their local longitudinal axis. Tr: trunk; In: introvert; L: length; W: width; T-L: total body length (trunk + introvert).

		Worm 1	Worm 2	Worm 3	Worm 4	Worm 5	Worm 6	Worm 7	Worm 8	Worm 9	Worm 10	Mean ± SD
Retracted	T-L	5.68 ± 0.09	3.90 ± 0.07	5.28 ± 0.06	5.3 ± 0.23	6.02 ± 0.06	11.10 ± 0.60	14.70 ± 1.30	12.10 ± 0.35	15.80 ± 0.75	8.80 ± 0.60	8.87 ± 4.30
	Tr-L	4.41 ± 0.13	3.32 ± 0.09	4.14 ± 0.07	4.87 ± 0.24	4.65 ± 0.11	9.20 ± 1.17	12.40 ± 1.58	11.10 ± 0.46	10.90 ± 1.03	7.60 ± 0.67	7.26 ± 3.40
	In-L	1.27 ± 0.10	0.58 ± 0.05	1.14 ± 0.03	0.43 ± 0.08	1.37 ± 0.09	1.90 ± 1.00	2.30 ± 0.90	1.00 ± 0.30	4.90 ± 0.70	1.20 ± 0.30	1.61 ± 1.28
	Tr-W	1.52 ± 0.04	0.93 ± 0.05	2.00 ± 0.03	1.13 ± 0.07	1.41 ± 0.01	3.20 ± 0.10	2.40 ± 0.10	1.80 ± 0.20	2.90 ± 0.20	1.80 ± 0.30	1.91 ± 0.74
	In-W	1.10 ± 0.05	0.49 ± 0.05	1.19 ± 0.00	0.88 ± 0.02	1.18 ± 0.09	1.84 ± 0.26	1.53 ± 0.25	1.46 ± 0.16	2.08 ± 0.52	1.31 ± 0.34	1.31 ± 0.46
Extended	T-L	15.13 ± 0.31	9.63 ± 0.66	10.56 ± 0.40	10.81 ± 0.99	18.56 ± 0.17	22.10 ± 1.10	31.80 ± 1.90	23.60 ± 1.70	26.10 ± 2,40	19.20 ± 1.00	18.75 ± 7.35
	Tr-L	5.59 ± 0.40	3.68 ± 0.86	3.38 ± 0.98	4.30 ± 1.01	6.17 ± 0.64	9.30 ± 2.02	12.90 ± 3.22	10.50 ± 2.55	11.20 ± 4.33	10.00 ± 1.72	7.70 ± 3.47
	In-L	9.54 ± 0.26	5.95 ± 0.55	7.18 ± 0.90	6.51 ± 0.18	12.39 ± 0.62	12.80 ± 1.70	18.90 ± 2.60	13.10 ± 1.90	14.90 ± 3.60	9.20 ± 1.40	11.05 ± 4.12
	Tr-W	1.03 ± 0.05	0.77 ± 0.04	1.56 ± 0.10	0.94 ± 0.02	1.04 ± 0.07	2.90 ± 0.20	1.80 ± 0.20	1.60 ± 0.10	2.70 ± 0.40	1.50 ± 1.00	1.58 ± 0.72
	In-W	0.86 ± 0.09	0.46 ± 0.01	1.16 ± 0.14	0.77 ± 0.02	0.83 ± 0.05	1.39 ± 0.13	1.19 ± 0.23	0.93 ± 0.05	1.10 ± 0.10	0.84 ± 0.10	0.95 ± 0.26

Table 1. Biometric measurements (mean ± SD, standard deviation) obtained from ten individuals of *P. stephensoni* collected from shallow rocky shores, measured in both retracted and extended states (see Fig. 3). Tr: trunk; In: introvert; L: length; W: width; T-L: total body length (i.e., trunk + introvert).

of the trunk approximates a cylinder with a constant length, even small reductions in circumference due to the action of trunk circular muscles produce significant fluid volume displacement and elongation of the introvert ($V \propto r^2$). Retraction of the introvert into the trunk is achieved via specialized retractor muscles (two dorsal and two ventral) which attach anteriorly to the distal extremity of the introvert, near the perioral region, and posteriorly to the inner body wall of the trunk (Fig. 2). These muscles enable rapid and forceful retraction, a critical defense mechanism against predation. In contrast, the longitudinal muscles of the body wall are thought to contribute to body stiffening, bending control, and stabilization during introvert extension and movement, but their role appears to be secondary in generating large-scale motion.

Morphological variation among individuals in *P. stephensoni* is relatively limited compared to other annelids though differences in body size and introvert-to-trunk ratio are observed (Fig. 3; Table 1). Notably, some of these differences appear to be associated with local ecological adaptations. For instance, individuals collected from natural rocky substrates were consistently smaller and exhibited a smoother external texture compared to conspecifics found in port environments, particularly those inhabiting sponges[26], highlighting the importance of environmental interactions in shaping the structural traits of the organism (see Supplementary Figure S1).

Morphological analyses based on high-resolution image analysis across retraction and protrusion states in ten individuals collected from shallow rocky shores revealed a clear functional distinction between the trunk and the introvert (Fig. 3; Table 1). Specifically, the lengths of the trunk and introvert were measured along the curvilinear longitudinal axis of each respective region, whereas widths were recorded at the midpoint of each portion, perpendicular to the local longitudinal axis in both retracted and extended configurations. Total body length in the protruded state increased to slightly more than twice that measured in the retracted configuration, and quantitative measurements clarified the respective contributions of the trunk and introvert to overall body shape change. Trunk morphology remained highly stable across configurations, as indicated by consistent measurements of trunk dimensions (length: 7.26 ± 3.40 mm in the retracted state vs. 7.70 ± 3.47 mm in the extended state, corresponding to a + 6.1% change; width: 1.91 ± 0.74 mm in the retracted state vs. 1.58 ± 0.72 mm in the extended state, corresponding to a – 17.3% change) and confirmed its predominantly cylindrical shape. In contrast, the introvert underwent pronounced morphological changes during protrusion (length: 1.61 ± 1.28 mm in the retracted state vs. 11.05 ± 4.12 mm in the extended state, corresponding to a + 586%

increase; width: 1.31 ± 0.46 mm in the retracted state vs. 0.95 ± 0.26 mm in the extended state, corresponding to a − 27.5% reduction), and its width decreased as it everted from the trunk, consistent with a more conical geometry compared to the trunk.

Further analysis of the results in Table 1 showed that elongation capacity was also influenced by body size. Although retracted and extended total body lengths are strongly linearly correlated (R^2 = 0.98; Fig. 4a), indicating that body elongation scales with size, inspection of individual data reveals size-dependent differences in relative elongation. Smaller individuals tend to lie above the regression line, exhibiting proportionally greater elongation with extended lengths approaching three times their retracted size, whereas larger specimens cluster closer to the regression trend, showing lower relative elongation ratios despite greater absolute extension. Partitioning total elongation into regional contributions further showed that the trunk exhibited only minor deformation during protrusion and, in some cases, appeared marginally shorter in the extended state than in the retracted configuration. This limited contribution is reflected in the near-unity slope of the linear regression relating extended to retracted trunk length (slope ≈ 1.08), indicating minimal length change (Fig. 4b). By contrast, the introvert showed substantial apparent elongation, as confirmed by the much higher regression coefficient (slope ≈ 8.09; Fig. 4c), reaching on average nearly eight times its visible length in the retracted state. However, this value does not reflect true tissue elongation, but rather results from the eversion of the distal portion of the introvert that remains folded within the trunk during contraction and becomes exposed at the tip during protrusion, and therefore cannot be directly quantified in the retracted configuration. Analysis of radial deformation mirrored the patterns observed for longitudinal elongation (Fig. 4d and e). The trunk displayed limited radial deformation, as reflected by a regression slope close to unity (slope ≈ 0.86; Fig. 4d), and consistent across specimens (R^2 = 0.99). In contrast, the introvert was more radially deformable, exhibiting a lower regression coefficient (slope ≈ 0.63; Fig. 4e) and greater inter-individual variability (R^2 = 0.97), consistent with the variability observed in its longitudinal extension.

To further quantify morphological changes during introvert retraction and protrusion, a subsequent micro-computed tomography (micro-CT) analysis was performed, enabling high-resolution characterization of both internal and external structural variations with greater anatomical precision. Representative micro-CT reconstructions of *P. stephensoni* in retracted, partially extended, and fully extended configurations are shown in Fig. 5. As expected, results revealed that body volume remained unchanged across configurations (Kruskal–Wallis, H = 4.34, p = 0.11), whereas significant differences were observed in body and retractor muscle lengths (Table 2). Specifically, body length (11.73 ± 2.39 in retracted state vs. 19.41 ± 6.95 in fully extended state corresponding

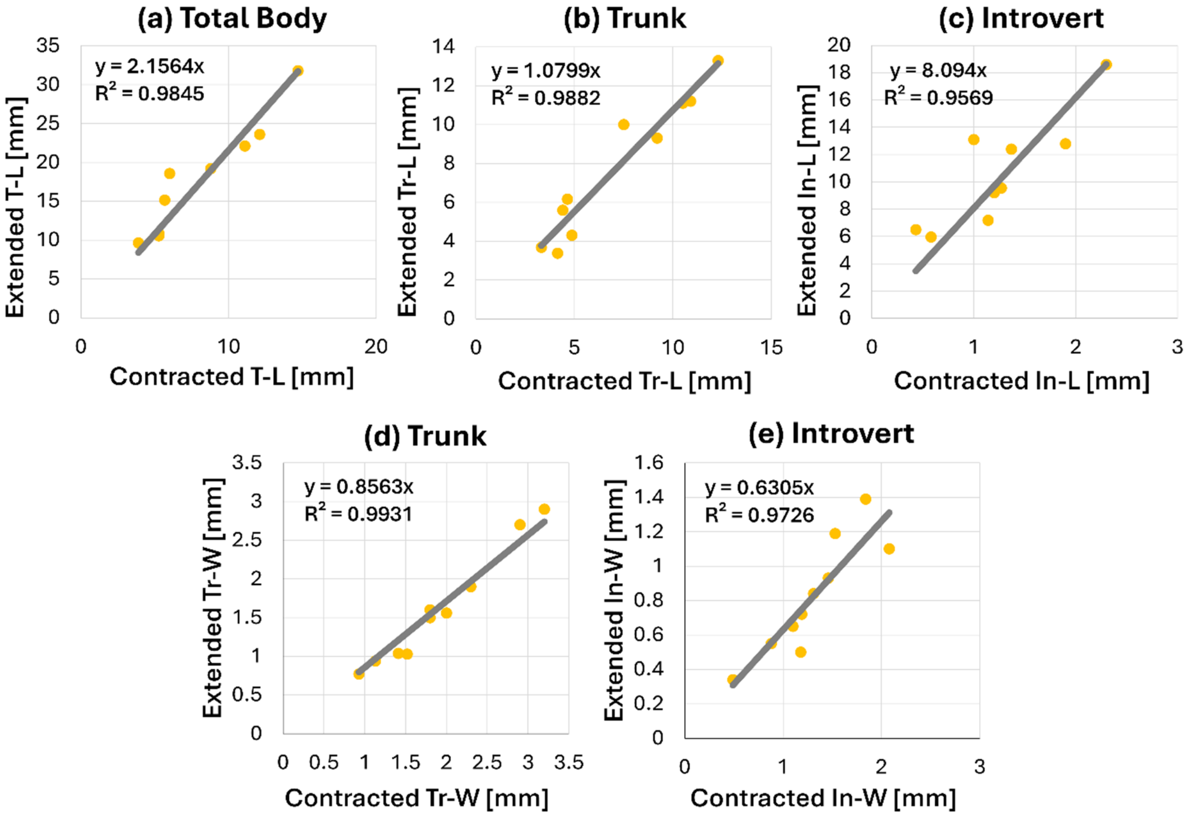

Fig. 4. Relationships between body dimensions measured in fully retracted and fully extended states in *P. stephensoni*. Panels show linear relationships between retracted and extended measurements for **a** total body length, **b** trunk length, **c** introvert length, **d** trunk width, and **e** introvert width. For each panel, the corresponding linear regression equation and trend line are reported. Tr: trunk; In: introvert; L: length; W: width; T-L: total body length (i.e., trunk + introvert).

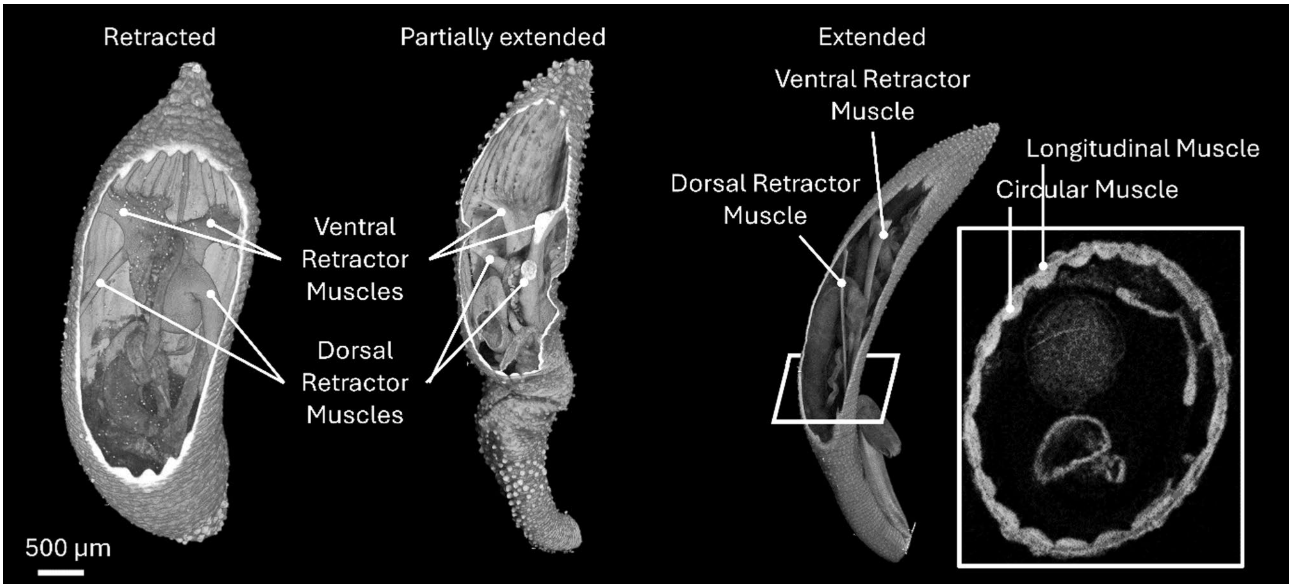

Fig. 5. Micro-computed tomography (micro-CT) scans of *P. stephensoni* illustrating the musculature in retracted (left), partially extended (center), and fully extended (right) introvert configurations. Ventral and dorsal retractor muscles are indicated in all three states. In the fully extended configuration, the inset shows a transverse section detailing the arrangement of longitudinal and circular muscles.

	B-L (mm)	dRM-L (mm)	vRM-L (mm)	V (mm^3)	dRM-t (μm)	vRM-t (μm)	LM-t (μm)	CM-t (μm)
Retracted	11.73 ± 2.39	6.167 ± 0.89	8.198 ± 1.24	25.25 ± 1.64	342.99 ± 38.77	246.71 ± 24.81	159.13 ± 78.66	46.59 ± 18.18
Partial extended	11.59 ± 1.72	8.3 ± 0.86	9.14 ± 0.86	20.2 ± 11.7	281.24 ± 36.4	210.69 ± 7.58	96.46 ± 40.25	35.94 ± 9.29
Extended	19.41 ± 6.95	11.72 ± 2.15	12.66 ± 2.2	23.3 ± 19.5	196.1 ± 119.81	161.2 ± 76.32	65.16 ± 16.58	30.78 ± 1.91

Table 2. Biometric measurements (mean ± SD, standard deviation) obtained from micro-computed tomography (micro-CT) scans of individuals of *P. stephensoni* across three functional configurations (see Fig. 5.): retracted (3 replicates), partially extended (4 replicates), and fully extended (6 replicates) introvert. The parameters measured included total body length (B-L) and the length of the dorsal and ventral retractor muscles (dRM-L and vRM-L). In addition, the total body volume (V), the dorsal and ventral retractor muscle thickness (dRM-t and vRM-t), longitudinal muscle thickness (LM-t), and circular muscle thickness (CM-t) were quantified.

to a + 65.5% increase; H = 8.18, $p = 0.017$), dorsal retractor muscle length (6.17 ± 0.89 mm vs. 11.72 ± 2.15 mm, corresponding to a + 90.0% increase; H = 9.69, $p = 0.008$), and ventral retractor muscle length (8.20 ± 1.24 mm vs. 12.66 ± 2.20 mm, corresponding to a + 54.4% increase; H = 8.79, $p = 0.01$) all showed statistically significant changes. Post-hoc comparisons, conducted using Dunn's test with Bonferroni correction, are presented in Table S1 in the Supplementary Materials, which reports the comparisons among the different body configurations for the various biometric measurements. Retraction and protrusion movements also affected retractor muscle thickness (Table 2, see also Fig. 2); however, these changes were not statistically significant (dorsal: H = 3.30, $p = 0.19$; ventral: H = 4.58, $p = 0.10$).

Biomechanical properties of soft tissues

Analysis of the biomechanical properties of trunk and introvert tissues in seawater reinforced the distinction identified through biometric measurements, confirming that the two body regions are mechanically specialized to support different functional demands. The tests were performed in seawater to ensure that the tissues were assessed under conditions that closely replicate their natural, functional configuration, providing the most realistic evaluation of their mechanical properties. Additionally, to assess whether testing conditions could influence the mechanical results, we conducted a preliminary control experiment in air (outside water) on a single specimen, and comparison with the data obtained in seawater showed no significant differences in mechanical response, except for a faster and more pronounced deterioration observed in air (see Supplementary Materials, Figure S2 and Table S3). Specifically, the trunk and introvert exhibit distinct yet comparable biomechanical responses, with overlapping stress–strain ranges that reflect shared tissue composition but different functional roles (Fig. 6). Monotonic uniaxial tensile tests to failure performed on three trunk samples and three introvert samples indicate that the introvert is generally less stretchable than the trunk, failing at strains up to approximately 60–65% (with one specimen failing at 41%), whereas the trunk can sustain larger deformations, reaching strains up to 90–110%

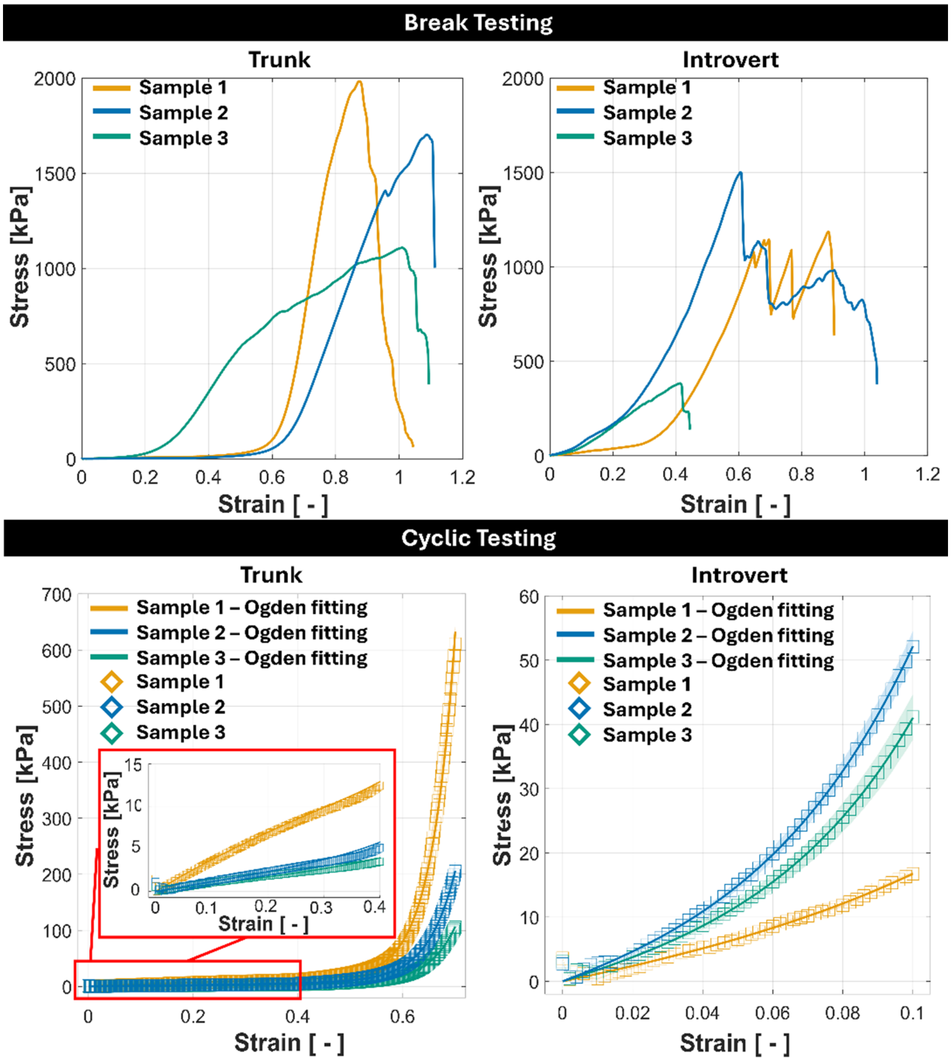

Fig. 6. Stress–strain curves of trunks and introverts from three different worms obtained from (up) monotonic tensile tests to failure and (bottom) cyclic tensile tests (40 cycles of uniaxial extension up to 70% strain for the trunk and 10% strain for the introvert). All uniaxial tensile tests were conducted using an Instron testing machine at a constant elongation rate of 1 mm/s.

before failure. Failure stresses were of comparable order of magnitude for the two tissues, with peak values in the range of ~0.5–2 MPa. However, the trunk consistently withstood moderately higher stresses than the introvert (mean ± SD: 1595 ± 441 kPa for the trunk and 981 ± 564 kPa for the introvert), despite substantial inter-sample variability. Beyond differences in ultimate strain, the stress–strain curves reveal a nonlinear mechanical response for both tissues, characterized by an initially compliant regime followed by progressive stiffening at higher strains. This behavior is consistent with the progressive recruitment and alignment of fibrous components within the tissue matrix, as well as the contribution of muscular elements within the composite tissue structure, as commonly observed in soft biological tissues.

Cyclic tensile tests (40 cycles of uniaxial extension up to 70% strain for the trunk and up to 10% strain for the introvert) showed reproducible loading–unloading behavior, with limited hysteresis and no evident mechanical degradation over repeated cycles. This response indicates good elastic recovery and mechanical stability within the tested deformation ranges. Notably, the trunk exhibited a wider elastic operating window and lower relative stiffness at small strains, whereas the introvert showed a comparatively stiffer response even at low deformation levels, consistent with their distinct functional roles. Indeed, the relatively limited extensibility of the introvert supports the interpretation that introvert protrusion primarily relies on eversion at the tip driven by hydrostatic pressure, with tissue stretching playing a secondary role.

To quantitatively capture this nonlinear behavior, stress–strain data from cyclic tests were fitted using an Ogden hyperelastic model implemented in MATLAB. The fitting procedure successfully reproduced the experimental trends for all samples, yielding high coefficients of determination ($R^2 \geq 0.98$, Table S2), thereby confirming the suitability of this constitutive model to describe the mechanical response of both trunk and introvert tissues and providing a robust basis for subsequent biomechanical modeling and soft robotic translation.

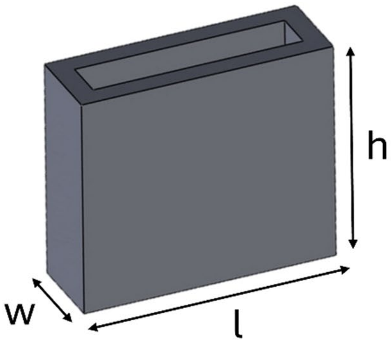

	Height (h) [mm]	Length (l) [mm]	Width (w) [mm]
Aquarium 1	50	50	4
Aquarium 2	50	50	7
Aquarium 3	50	50	10
Aquarium 4	100	100	4
Aquarium 5	100	100	7
Aquarium 6	100	100	10

Fig. 7. Schematic representation of the different aquarium dimensions used during the experimental tests. Two combinations of height (h) and length (l) were tested in gel experiments, namely l = h = 50 mm and l = h = 100 mm, in order to investigate the influence of confinement and available penetration distance on the measured mechanical response of the gel. In contrast, aquariums with dimensions of 100 × 100 mm^2 were used for the experiments involving live worms.

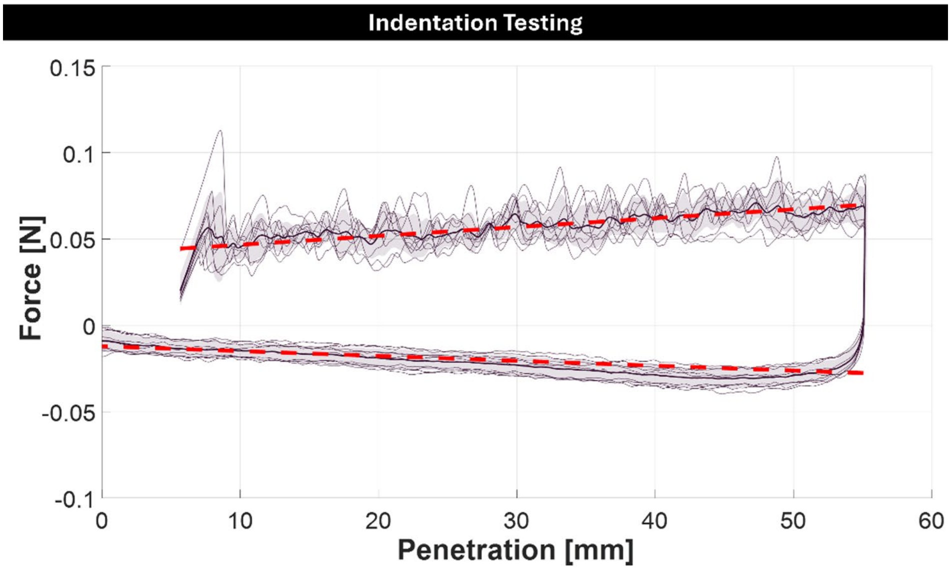

Fig. 8. Axial force as a function of penetration depth measured during loading and unloading indentation tests in a 0.5 wt% agarose gel. Data correspond to a representative experimental condition with penetration speed v = 5 mm/s, aquarium width w = 7 mm, and aquarium height and length l = h = 100 mm. Thin gray curves represent individual experimental trials, while the thick dark curve shows the averaged force–depth response and dashed red lines indicating the linear regressions fitted to the data. The low slope of the force–depth curves highlights the weak dependence of axial force on penetration depth under these conditions.

Aquaria characterization

To quantitatively interpret the biomechanical behavior of worms, experiments were conducted in narrow, gel-filled aquaria designed to strongly confine their motion (small aquaria: length and height equal to 50 mm; large aquaria length and height equal to 100 mm; three widths: 4 mm, 7 mm, and 10 mm; Fig. 7). This geometric confinement restricted worm movement to approximately two dimensions, enabling more accurate observation and extraction of shape, locomotion, and eversion kinematics from video recordings. As a consequence of this confinement, the mechanical properties of the experimental aquaria were characterized through indentation tests at four penetration velocities (v = 0.5, 1.0, 5.0, and 10.0 mm/s) to quantify the forces acting during worm movements involving local deformation, fracture, and rearrangement of the gel network, which generate resistive forces that directly couple to the worms' internally generated muscular forces. Specifically, tests were carried out in the aquaria filled with 0.5% agarose gel prepared in filtered seawater, which was identified as the best choice among different substances (including sodium alginate and glycerol).

During indentation of the gel, the axial force exhibited a slightly irregular variation, as indicated by the low slope of the force–depth curve shown in Fig. 8, obtained for a representative experimental condition with penetration speed $v = 5$ mm/s, aquarium width $w = 7$ mm, and aquarium height $h = 100$ mm. Over the tested penetration range, the axial force increased only mildly, with values rising from about 0.04 N to approximately 0.07 N during loading, while the unloading phase displayed a comparable trend with opposite sign. The corresponding slopes of the loading and unloading curves are small, indicating a weak dependence of axial force on penetration depth. This weak dependence suggests that the contribution of viscous forces acting on the lateral surface of the indenter is negligible; consequently, the measured axial force primarily reflects the tip force required to locally break the gel network and allow forward advancement. The limited hysteresis between loading and unloading curves further supports the interpretation of a predominantly fracture-dominated response, with minor rate-dependent dissipation.

Aquarium size and penetration speed also influence the measured axial force, revealing a combined effect of geometric confinement and rate-dependent mechanical response of the gel as shown in Fig. 9. At low penetration speeds (0.5–1 mm/s), higher forces are observed in the 7 mm-wide aquarium (approximately 0.05–0.1 N), whereas lower forces are measured in both the 4 mm- and 10 mm-wide aquaria. This dependence on confinement becomes less pronounced at higher speeds, where the axial force generally exceeds 0.1 N and shows no significant variation across different aquarium widths. This behavior suggests a weakly viscous mechanical response of the gel, which can be captured, to a first approximation, by four parameters: the slopes and intercepts of the linear regressions of the loading and unloading force–depth curves, as previously highlighted in Fig. 8.

Peristaltic locomotion

Despite the absence of segmentation, sipunculans are capable of peristaltic locomotion, which emerges from coordinated, traveling waves of contraction and relaxation along their continuous body wall. In this segment-free system, peristalsis is generated by the sequential activation of circular and longitudinal muscles, which locally modulate body diameter, internal pressure, and frictional interactions with the surrounding substrate. These coordinated deformations give rise to a propagating wave along the body axis, enabling forward displacement without reliance on discrete segments and highlighting an alternative strategy for peristaltic locomotion based on continuous deformation.

To quantitatively capture and rationalize this mechanism, peristaltic locomotion of *P. stephensoni* was modeled by representing the worm as a one-dimensional continuous body undergoing prescribed spatio-temporal strain patterns that mimic muscular activation. The resulting framework links internal deformation waves to net forward motion through interactions with the surrounding medium. Specifically, we modeled the worm as a 1D rod moving along a straight line, subject to gravity and immersed in a medium of viscosity μ. Following previous works,23,24,25 the reference configuration is the segment $[X_1 := 0, X_2 := L]$, where L is the length of the worm in its relaxed state, and a generic point along it will be denoted by *X*. For any given point *X* in the reference configuration, the current position *x(X, t)* is written as:

$$x\left(X,t\right)=x\left(X_1,t\right)+s\left(X,t\right)=x_1\left(t\right)+s\left(X,t\right),\forall X\in\left[0,L\right],$$

where $s(X,t)$ is the arc-length in the deformed configuration at time *t*, i.e., the current distance of point *X* from the origin X_1, which describes the current shape of the worm. By definition, $s\left(0,t\right)\equiv 0$ and we assume:

$$s'\left(X,t\right):=\frac{\partial s(X,t)}{\partial X}>0,\forall X\in[0,L].$$

To reproduce the muscular activation of the worm, the rod is assumed to contract and expand with a certain periodicity and wave shape. To model this behavior, we impose a current shape of the worm-rod through the arc-length *s*, that is:

$$s'\left(X,t\right)=\gamma^{\star}\left(X,t\right)>0,\forall X\in\left[0,L\right],$$

where $\gamma^{\star}$ is a function expressing the contraction pattern of the worm in terms of strains.

Assuming negligible inertia for moving worms (for example, low Reynolds numbers in the case of self-propulsion within a fluid medium), force balance reduces to:

$$F_f\left(t\right)+F_e\left(t\right)=0,$$

where $F_f\left(t\right)$ denotes the total frictional force acting on the worm due to the viscous fluid, while $F_e\left(t\right)$ is the component along the axis of motion of external body forces, e.g., gravity. We describe the distributed frictional forces $f\left(x,t\right)$ through a p-model given by:23

$$f\left(x,t\right):=-\mu\big(s'\left(X,t\right)\big)^{-p}v\left(x,t\right),$$

where *X* is the reference point located at position *x*, and:

$$v\left(x,t\right)=\dot{x}\left(X,t\right)|_{X=s^{-1}(x(t)-x_1(t),t)}=\dot{x}_1\left(t\right)+\dot{s}\left(s^{-1}\left(x\left(t\right)-x_1\left(t\right),t\right),t\right),$$

represents the spatial velocity at position *x* in the current configuration of the worm. Notably, as *p* becomes large, the model approaches free slip in elongated regions (low friction when *s′* is large) and near-perfect grip in contracted regions (high friction when *s′* is small). The total frictional force can then be obtained via integration as:

(a) Indentation Testing Performed in small aquaria (l = h = 50 mm)

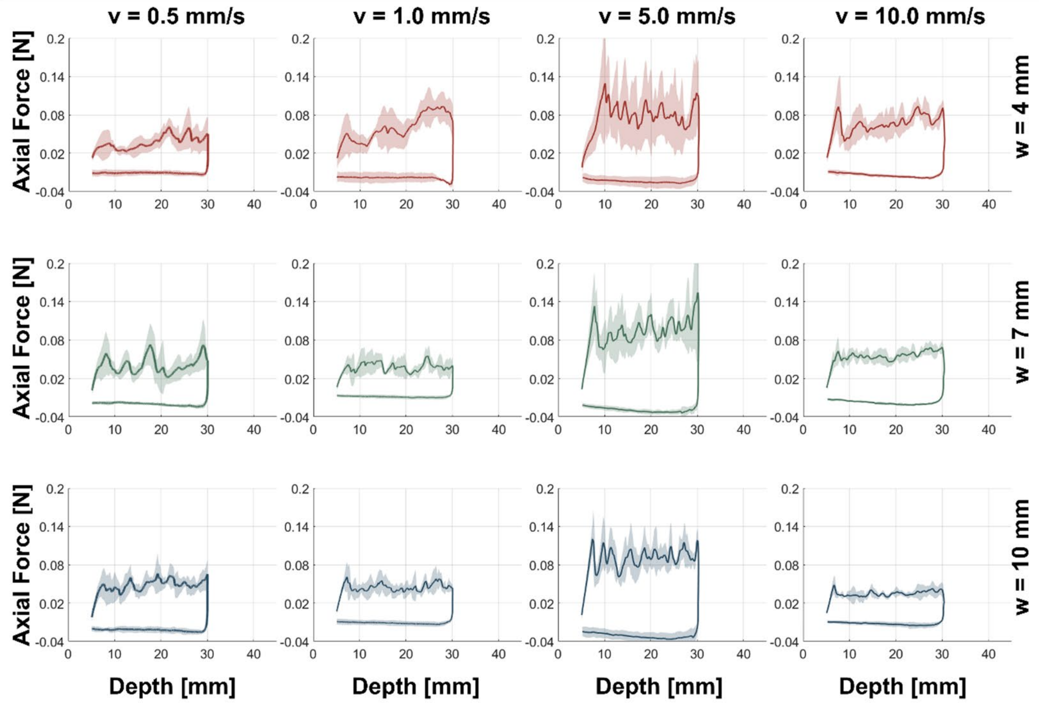

(b) Indentation Testing Performed in big aquaria (l = h = 100 mm)

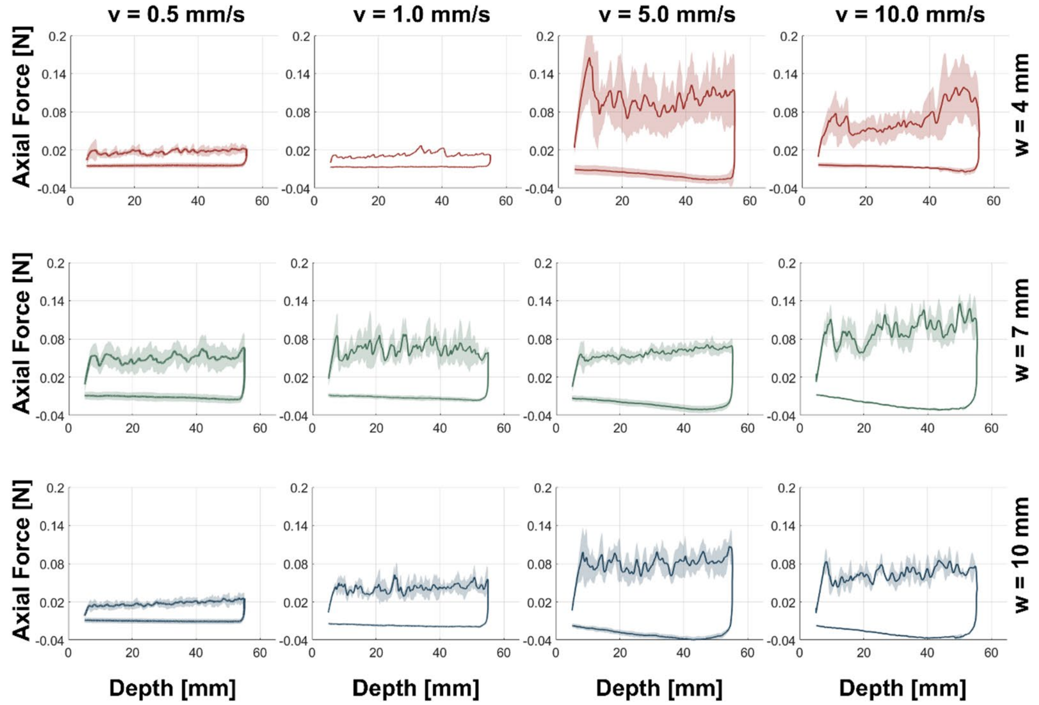

Fig. 9. Indentation tests performed in **a** small aquaria (length l = height h = 50 mm) and **b** large aquaria (l = h = 100 mm) filled with 0.5 wt% agarose gel prepared in filtered seawater. Three aquarium widths (w = 4 mm, 7 mm, and 10 mm) were considered. Tests were conducted at four penetration velocities (v = 0.5, 1.0, 5.0, and 10.0 mm/s). The plots show the axial penetration force during loading and unloading as a function of penetration depth.

$$F_f(t) = \int_{x_1}^{x_2} f(x,t)\,dx = \int_0^L f(x_1(t) + s(X,t), t) s'(X,t)\,dX.$$

Therefore, inserting the previous expressions into the force balance and rearranging, we obtain:

$$\dot{x}_1(t) = -\frac{\int_0^L (s'(X,t))^{1-p} \dot{s}(X,t)\,dX}{\int_0^L (s'(X,t))^{1-p} dX} + \frac{F_e(t)}{\mu \int_0^L (s'(X,t))^{1-p} dX}.$$

For assigned μ, $F_e(t)$, and $s'(X,t)$, the equation of motion of the 1D worm is then known.

Model predictions were quantitatively validated using a high-resolution video recording of a *P. stephensoni* moving within the custom-built experimental aquarium filled with 0.5% agarose gel prepared in filtered seawater, whose mechanical properties were previously characterized through indentation tests and explicitly incorporated into the model (Supplementary Video 1).

In the video, tail positions were tracked to extract precise displacement–time profiles. Quantitative comparison between experimental measurements and numerical simulations revealed a close agreement in both displacement magnitude and temporal evolution, with simulated trajectories accurately reproducing the stepwise forward progression observed experimentally (Fig. 10). Over the analyzed time window, model predictions captured the cumulative displacement within the same order of magnitude and followed the experimentally measured kinematics with minimal deviation. These results demonstrate that the proposed mathematical framework successfully links prescribed internal strain waves to net forward motion in a continuous, unsegmented body, thereby confirming its ability to reproduce peristaltic locomotion dynamics in sipunculan worms despite the absence of morphological segmentation.

Protrusion kinematics

To further investigate the biomechanical aspects of locomotion and digging in *P. stephensoni*, the speed of introvert protrusion and retraction was measured during burrowing behavior in the custom-built gel-filled aquaria. In agreement with previous literature and our expectations, the trunk was observed to passively follow the motion of the introvert during digging and, in most cases, did not actively contribute to propulsion. Consequently, only introvert movement was considered in the subsequent analyses. Both protrusion and retraction speeds varied with aquarium size. In the 4 mm-wide aquarium, the average protrusion speed was 0.76 ± 0.09 mm s^{-1}; in the 7 mm-wide aquarium, it increased to 1.13 ± 0.39 mm s^{-1}; and in the 10 mm-wide aquarium, it decreased to 0.44 ± 0.06 mm s^{-1} (Table 3; Fig. 11). Retraction speed followed a similar trend: the average value was 0.38 ± 0.18 mm/s in the 4 mm-wide aquarium, 1.79 ± 0.82 mm/s in the 7 mm-wide aquarium, and 0.40 ± 0.17 mm/s in the 10 mm-wide aquarium. In all cases, both protrusion and retraction speeds were highest in the 7 mm-wide aquarium, indicating the presence of an intermediate mechanical regime in which the balance between gel resistance and deformability favors efficient burrowing for average-sized individuals of *P. stephensoni*. Notably, the 7 mm-wide aquarium also corresponded to the confinement condition exhibiting the highest axial forces during indentation tests (Fig. 9). This apparent increase in force requirement does not hinder locomotion; rather, it suggests that the higher resistance of the gel under intermediate confinement enables greater stress accumulation and more effective force transmission along the axis of motion. As a result, gel

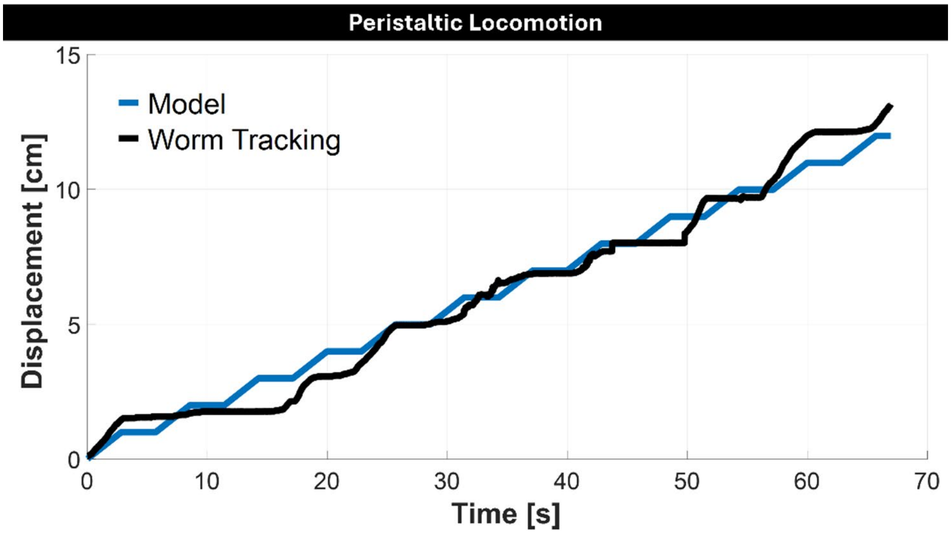

Fig. 10. Comparison between model-predicted displacement and experimental measurements obtained by tracking a live *P. stephensoni* during peristaltic locomotion. Displacement over time is shown for the numerical model (blue line) and the experimentally tracked worm (black line), highlighting the close agreement between simulated and observed locomotor dynamics.

	4 mm-wide aquarium	7 mm-wide aquarium	10 mm-wide aquarium
Protrusion	0.76 ± 0.09	1.13 ± 0.39	0.44 ± 0.06
Retraction	0.38 ± 0.18	1.79 ± 0.82	0.40 ± 0.17

Table 3. Protrusion and retraction speeds of the introvert measured during burrowing in agarose-filled aquaria of different widths (4, 7, and 10 mm). Values are reported as mean ± standard deviation across five individuals for each experimental condition. All speeds are expressed in mm s^{-1}.

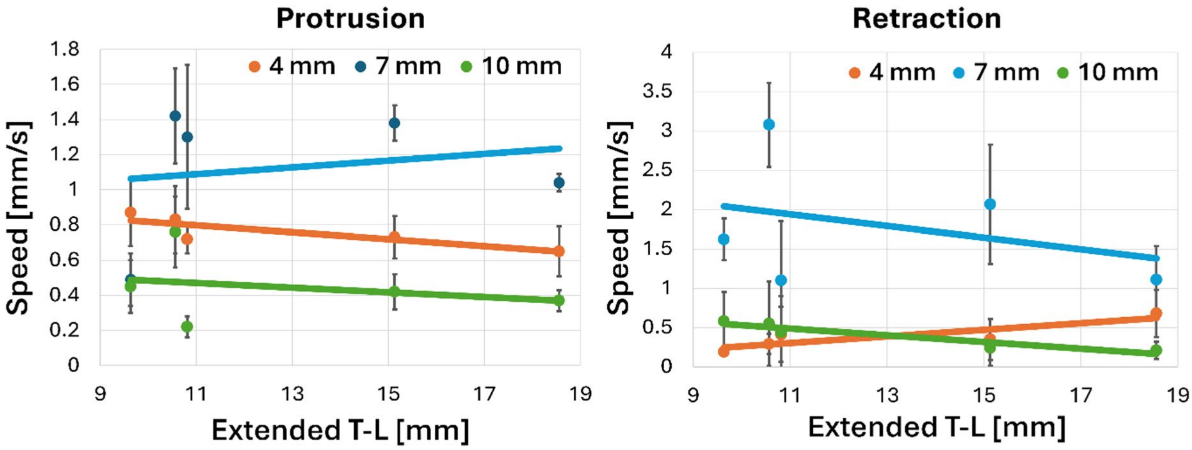

Fig. 11. Relationship between extended total body length and introvert protrusion (left) and retraction (right) speeds in *P. stephensoni* measured in the three experimental aquaria (4, 7, and 10 mm width) filled with 0.5% agarose gel prepared in filtered seawater. Data points represent mean speeds for individual worms, with error bars indicating standard deviation. For each worm in each experimental condition, five different speed estimates were obtained. Solid lines show linear regressions fitted to the data for each aquarium width. T-L: total body length (i.e., trunk + introvert).

fracture and yielding at the tip could be more localized and directionally aligned with forward extension, leading to faster protrusion and retraction. By contrast, in the 4 mm-wide aquarium, strong confinement may restrict gel rearrangement and prevent effective stress accumulation ahead of the tip, potentially leading to premature or poorly directed yielding and increased functional opposition to forward motion despite lower forces measured during indentation. Conversely, in the 10 mm-wide aquarium, the lower level of confinement may result in a more compliant surrounding medium, potentially promoting lateral, non-productive deformations and increased energy dissipation, thereby reducing the effectiveness of force transmission and overall burrowing performance. Based on these observations, all subsequent measurements were conducted in the 7 mm-wide aquarium.

No clear relationship between body size and either protrusion or retraction speed was detected, although larger individuals appeared capable of achieving higher absolute speeds (Fig. 11). Finally, introvert speeds measured within the gel were compared with those recorded in seawater outside the gel. However, speed values under these two conditions were broadly comparable and exhibited substantial variability, likely reflecting the influence of additional behavioral and environmental factors (Fig. 12).

Potential application: magnetically driven soft robots

To demonstrate the potential of this bioinspired approach, we focused on the protrusion of the proboscis, a hallmark behavior enabled by the worm's anatomical organization and tissue heterogeneity. We sought to replicate this mechanism by designing a soft, worm-like robotic structure composed of materials with carefully selected and spatially distributed stiffness, combined with magnetically responsive properties (Fig. 13). The worm-inspired system consists of a fluid-filled trunk that mimics the hydrostatic skeleton of the biological organism and a passive, eversible introvert positioned inside the trunk in the retracted state. The trunk has a bulged square prism shape (30 mm in height, with a rounded-square cross-section and a corner radius of 4 mm), while the introvert has a 45 mm long and 200 µm thick conical shape. The trunk comprises four 2 mm-thick magnetically responsive regions (15 mm × 30 mm). The magnetic regions consist of a composite of DragonSkin-10 (Shore Hardness 10 A) silicone mixed with 5 µm neodymium–iron–boron (NdFeB) particles in a 1:1 weight ratio and, thanks to their specific magnetization profiles, bend when an external magnetic field is applied along Z direction (Fig. 14). Indeed, the magnetic regions were magnetized in a folded configuration using an impulse magnetizer applying a 3.5 T magnetic field, such that the two lengthwise halves exhibited opposite magnetization directions along their thickness. Additionally, each region incorporates a central notch aligned with the intended bending axis, which locally reduces bending stiffness, and enables larger bending angles under magnetic actuation. When

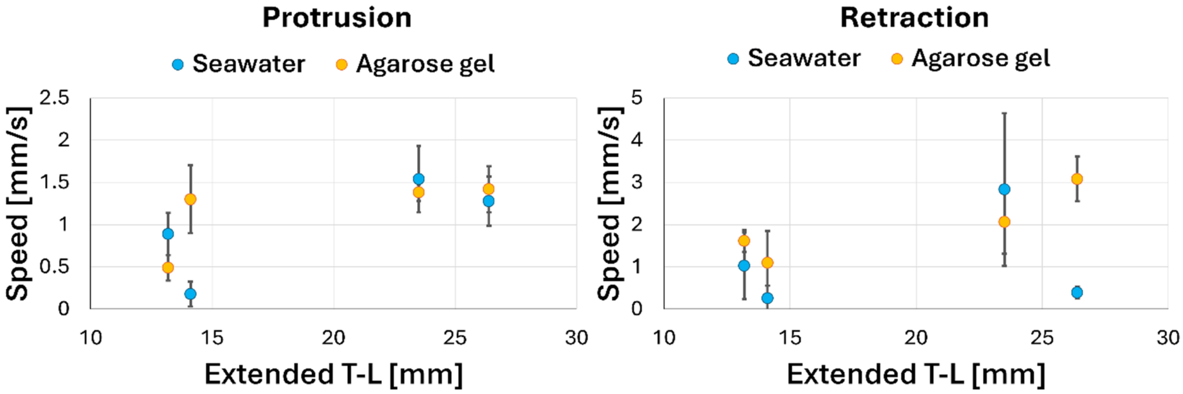

Fig. 12. Comparison of relationship between extended total body length and introvert protrusion (left) and retraction (right) speeds in *P. stephensoni* measured during burrowing in seawater and in 0.5% agarose gel prepared in filtered seawater. Data points represent mean speeds for individual worms, with error bars indicating standard deviation. For each worm in each experimental condition, five different speed estimates were obtained. T-L: total body length (i.e., trunk + introvert).

the four magnetically responsive regions bend, they collectively compress the internal fluid (20 mL of water) contained within the trunk. This deformation reduces the local trunk diameter and generates an internal pressure increase that drives fluid toward the introvert, thereby inducing its eversion. This mechanism closely replicates the function of circular muscles in the worm, which contract to decrease trunk diameter and hydraulically actuate protrusion through fluid redistribution. The introvert was designed to accommodate the fluid displaced by the trunk during actuation.

The material selection was guided by the biomechanical properties measured in the corresponding worm tissues (Figs. 6 and 15). Specifically, the introvert was fabricated using a relatively stiff silicone elastomer (DragonSkin-10, Shore hardness 10 A), enabling protrusion to occur primarily through material unrolling rather than through material stretching. This choice also effectively constrains radial expansion during protrusion without the need for additional external reinforcements or mechanical constraints. In contrast, the trunk was fabricated from an ultra-soft silicone elastomer (EcoFlex 00–10, Shore hardness 00–10), whose high compliance facilitates radial compression and fluid squeezing, mimicking the deformability of the worm's trunk tissues. Although EcoFlex 00–10 is intrinsically more compliant than the biological trunk tissue, this higher compliance was intentionally compensated by embedding four stiffer, magnetically responsive regions made of DragonSkin-10 loaded with 70 wt% NdFeB particles. These regions locally increase stiffness while enabling magnetic actuation. The use of a higher-stiffness silicone in the actuation units was mechanically necessary to enhance their output force during magnetically induced bending. Acting against the surrounding ultra-soft EcoFlex 00–10 structure, the particle-loaded regions effectively compress the trunk, thereby amplifying the hydraulic pressure generated within the structure and increasing the thrust that drives fluid into the introvert.

As shown in Fig. 15, the tensile tests performed on the selected silicones highlight a clear quantitative difference in mechanical response between the two selected silicones. DragonSkin-10 reaches stresses of approximately 2 MPa before failure at moderate strains ($\varepsilon \sim 3–4$). In contrast, EcoFlex 00–10 remains below 1 MPa even at very large strains ($\varepsilon \sim 7$), with a significantly lower initial tangent modulus. Within the functional strain range relevant for robotic actuation ($\varepsilon < 2$), DragonSkin-10 consistently develops substantially higher stress levels than EcoFlex 00–10, as demonstrated by the cyclic tensile tests, confirming the intended stiffness contrast between the two materials. Indeed, EcoFlex 00–10 shows low stress levels (tens of kPa up to $\varepsilon \sim 2$) and a smooth, progressively stiffening response that is well captured by the Ogden hyperelastic fit ($R^2 \geq 0.98$, Table S4), reflecting its highly compliant nature. Conversely, DragonSkin-10 exhibits a much steeper stress–strain curve during cyclic loading (approaching ~ 900 kPa at $\varepsilon \sim 2$), also accurately described by the same constitutive model ($R^2 \geq 0.99$, Table S4).

Finally, to mimic the function of the retractor muscles, two passive, ultra-soft silicone strips (EcoFlex 00–10, Shore hardness 00–10; 20 mm × 2 mm × 400 µm) were symmetrically anchored between the tip of the introvert and the base of the trunk. These strips act as elastic elements that elongate during introvert protrusion and, upon reduction of the magnetic field, generate a restoring force sufficient to ensure rapid and complete withdrawal of the introvert.

Thanks to its smart architecture, upon full protrusion, the worm-inspired structure is able to elongate up to 2.5 times its initial body length when an external magnetic field of 250 mT is applied along the + Z direction, effectively replicating the large extensibility observed in biological worms (Fig. 13). Specifically, with this structural and material design, protrusion is driven by magnetic torque generated within the trunk's magnetically responsive regions (Fig. 14). Indeed, when an external actuating magnetic field (B_a) is applied along the Z direction, the misalignment between its direction and the magnetic moment (m_2) of the trunk's magnetic regions, generates a magnetic torque (τ_m) that drives the protrusion of the introvert equal to:

$$\tau_m = m_2 \times B_a$$

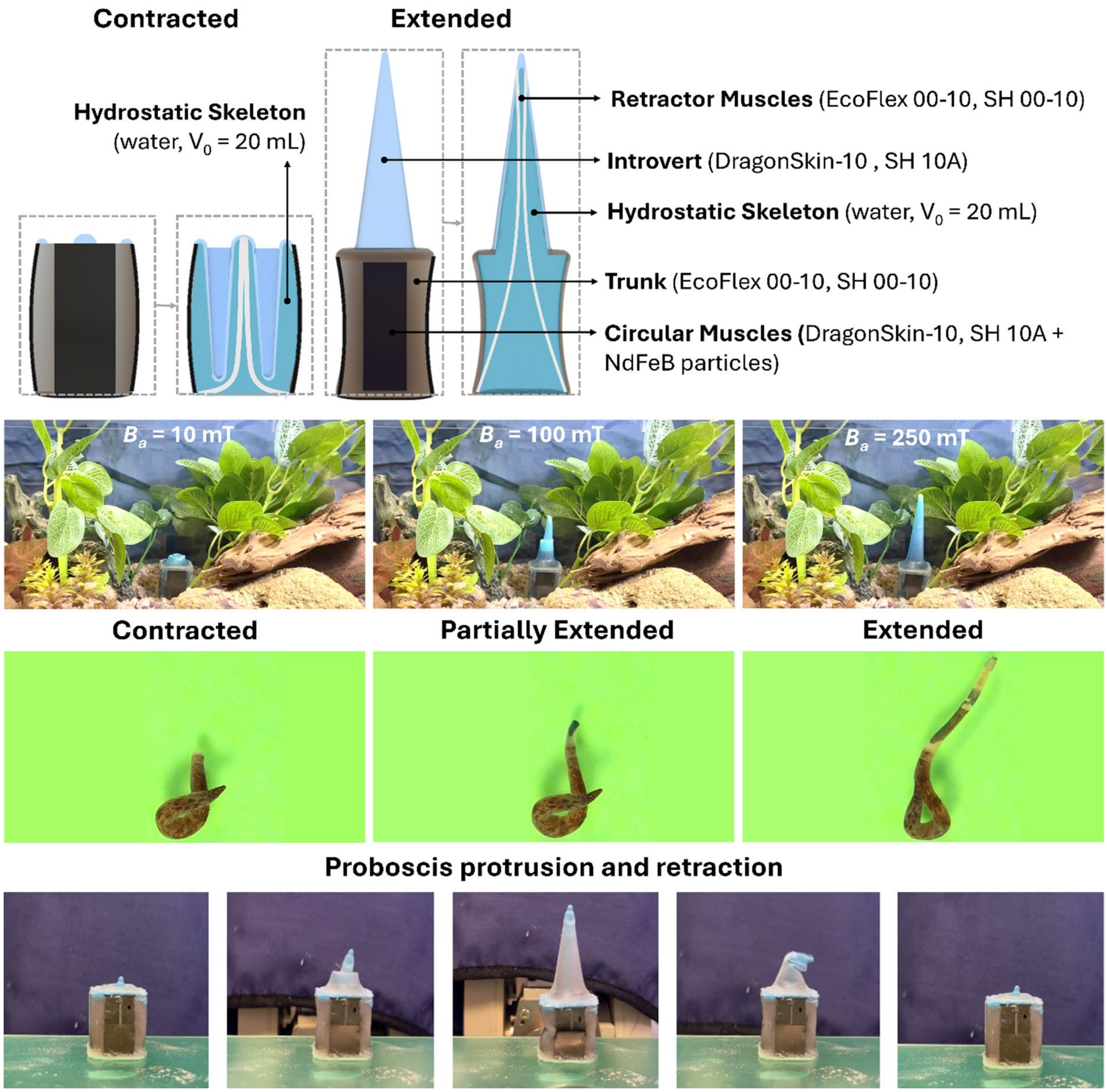

Fig. 13. Design and protrusion mechanism of the worm-inspired soft robotic structure. *Top*: Schematic representation of the structure in the retracted and fully extended states, highlighting the main functional components: hydrostatic skeleton filled with water (V_0 = 20 mL), stiff introvert (DragonSkin-10, Shore hardness 10 A), ultra-soft trunk (Ecoflex 00–10, Shore hardness 00–10), magnetically responsive regions mimicking circular muscles (DragonSkin-10, Shore hardness 10 A, embedded with NdFeB particles), and passive retractor muscles (Ecoflex 00–10). Protrusion is achieved through fluid redistribution within the artificial hydrostatic skeleton driven by trunk deformation under magnetic stimulation. *Center*: Sequential photographs illustrating the transition from the retracted to the partially extended and fully extended configurations, both in the soft robotic system actuated by an external magnetic field (B_a) and in the real worm. *Bottom*: Timelapse sequence showing proboscis protrusion in the soft robotic prototype.

As a result, each half of the magnetic bending units aligns its magnetic moment with the actuating magnetic field. Finite element simulations in COMSOL (Fig. 14c) further elucidate this mechanism. The simulations show the progressive increase in curvature as B_a increases (up to 50 mT in the model), together with the corresponding von Mises stress distribution within the elastomer. The highest stress concentrations are localized near the bending line of the magnetic segment, while the stress gradually decreases along the length. Importantly, the maximum simulated stresses remain well below the experimentally measured failure stresses of the particle-loaded silicone. To validate structural integrity, monotonic tensile break tests were performed on three independent samples of DragoSkin-10 with 70 wt% NdFeB particles. As shown in the experimental results (Fig. 14), the magnetic silicone composite reaches ultimate stresses on the order of ~ 10–11 MPa at strains approaching ~ 4 before failure, demonstrating substantial mechanical robustness. The stress levels predicted by the simulations (≤ 0.22 MPa in

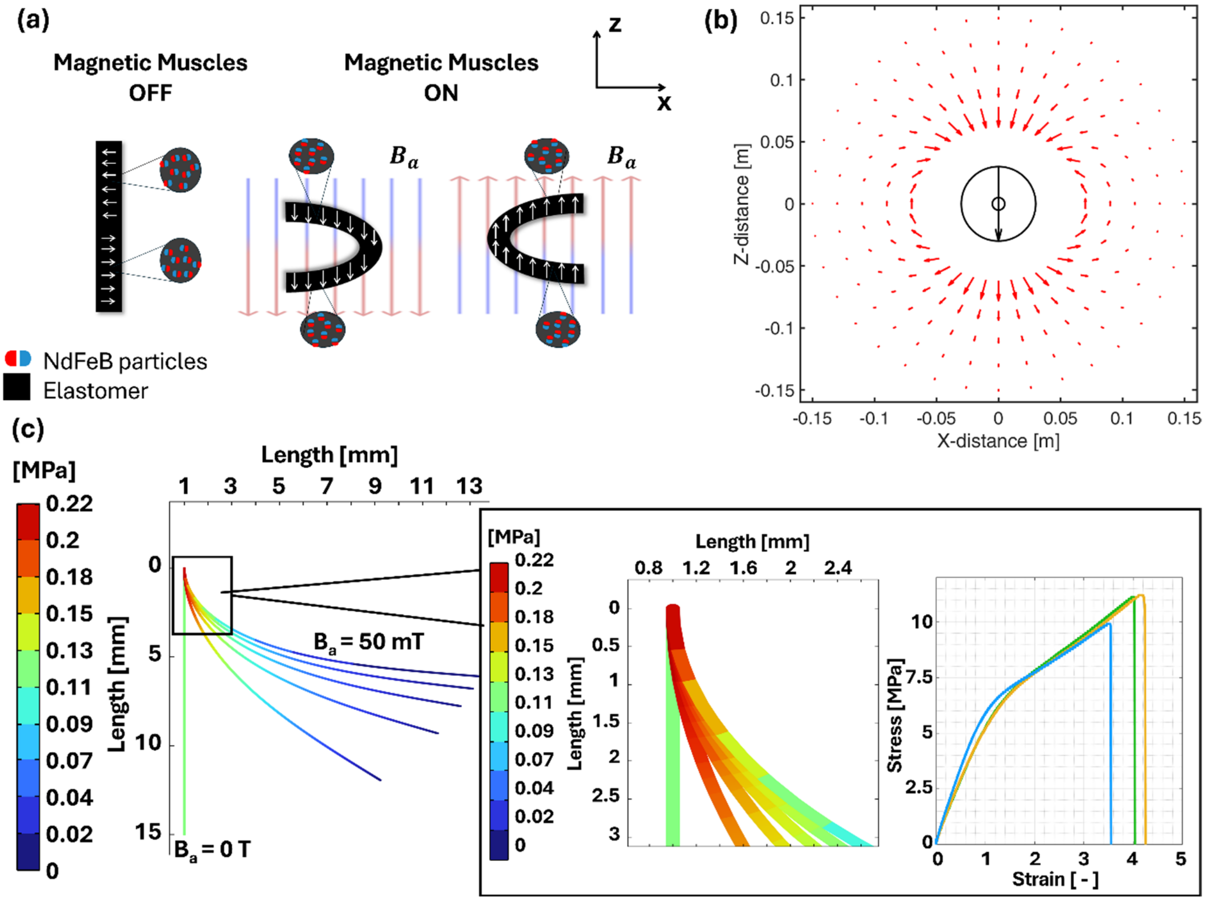

Fig. 14. **a** Schematic illustration of the magnetization and activation of the magnetically responsive regions embedded in the trunk, made of DragonSkin-10 loaded with 70 wt% NdFeB particles. When the magnetic field is off, the magnetic domains remain unaligned, whereas under an applied magnetic field (B_a) the NdFeB particles embedded in the elastomer align, generating bending of the magnetic region. **b** Spatial distribution of the magnetic field generated by a diametrically magnetized external permanent magnet (EPM). The arrows indicate the direction of the magnetic field, while their length represents the local field magnitude at each point in space. **c** Finite element simulations performed in COMSOL Multiphysics of half of a magnetically responsive region embedded in the trunk. Owing to geometric symmetry, only one half of the structure was modeled. The color map represents the von Mises stress distribution within the silicone composite as the bending angle increases in response to progressively higher vertically applied magnetic fields (B_a). The inset also reports the experimental monotonic tensile response to failure of DragonSkin-10 loaded with 70 wt% NdFeB particles.

bending) are therefore more than one order of magnitude lower than the measured failure strength, confirming a significant safety margin during magnetic actuation.

The bending deformation of the magnetic bending units squeezes the trunk and pushes the internal fluid into the introvert, driving its protrusion, like what the circular muscles do in the worms. In the experimental setting, the magnetic field applied along the Z-axis was controlled by varying the distance of a diametrically magnetized external permanent magnet (EPM) used as the magnetic field source. The distribution of magnetic field around the EPM in a plane perpendicular to its axis was calculated and shown in Fig. 14b where the direction of the red arrows represents the direction of the magnetic field, and the length of the red arrows represents the strength of the magnetic field. Specifically, the EPM can be approximated as a point dipole with a magnetic moment m_1 and, therefore, the magnetic field (B_a) at a point with position vector r can be calculated as:

$$B_a\left(r\right) = \frac{\mu_0}{4\pi}\left[\frac{3r\left(m_1 \cdot r\right)}{r^5} - \frac{m_1}{r^3}\right]$$

where μ_0 is the vacuum permeability constant. During experiments, the field intensity ranged between 10 mT and 250 mT.

Although preliminary, this proposed material-level design of the worm-inspired soft robot enabled untethered, wireless actuation without relying on rigid elements, embedded electronics, or complex control architectures. Indeed, the resulting functionality arises entirely from the physical intelligence encoded in the morphology and material properties of the structure itself, inspired by the worm analysis. By exploiting the

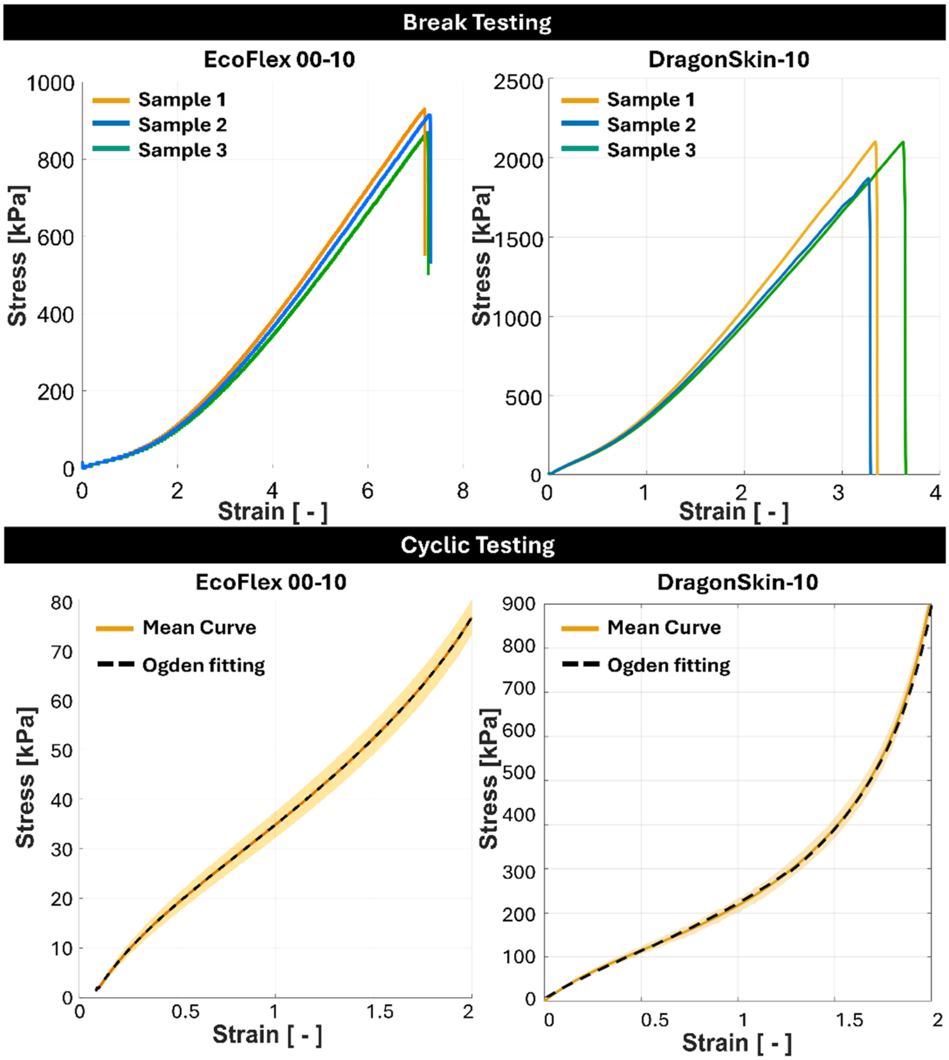

Fig. 15. Stress–strain curves of EcoFlex 00–10 and DragonSkin-10 obtained from (top) monotonic tensile tests to failure on three independent samples and (bottom) cyclic tensile tests. Shaded areas represent the experimental variability around the mean response, while dashed lines indicate the Ogden model fitting. All uniaxial tensile tests were performed under displacement-controlled conditions at a constant elongation rate of 200 mm/min.

intrinsic compliance, nonlinear mechanics, and magneto-responsive behavior of the constituent soft materials, the system reproduces eversion-driven shape changes through a passive, material-mediated interaction between magnetic field stimuli and the structure.

Discussion

Soft robotics has increasingly drawn inspiration from biological systems that exploit compliance, deformability, and embodied physical interactions with the surrounding to achieve complex behaviors in unstructured environments[1,5,25,30]. Previous studies have extensively investigated soft-bodied organisms such as annelid worms[31–33], insect larvae[34,35], and cephalopods[36,37], revealing how hydrostatic skeletons, distributed musculature, and environmental coupling can enable different locomotion strategies, grasping, and a wide range of other biomechanical functions. These analyses have informed a wide range of soft robotic designs, including worm-like robots[7,25,38–41], caterpillar-inspired crawlers[42,43],and octopus-inspired manipulators[44–47]. Focusing on worm-inspired robotics, a variety of actuation strategies have been explored, including pneumatic pressurization[48], tendon-driven mechanisms[49], shape-memory alloys[50], dielectric elastomers[51],and magnetic actuation[52]. However, despite this diversity of approaches, most existing designs focused on segmented architectures and largely relied on peristaltic locomotion achieved through the sequential activation of discrete body units.

More recently, growing interest has emerged around eversion-based soft robots[53], which exploit tip growth and pneumatic actuation to achieve elongation and navigation in confined environments. However, these systems typically rely on bulky and tethered actuation hardware. In this regard, biological systems that naturally combine eversion with locomotion may offer inspiration for alternative design principles capable of overcoming the limitations imposed by current designs. In this context, we identified unsegmented marine worms such as sipunculans as a largely unexplored source of bioinspiration. These organisms lack body segmentation yet achieve both peristaltic locomotion and extreme elongation through the eversion of their introvert tip. By focusing on such unsegmented worms, our study aims to expand the current bioinspired design space, highlighting biological strategies that may inform future soft robotic architectures capable of both locomotion and extreme shape change.

In this context, this study provides a quantitative, multiscale framework linking anatomy, tissue mechanics, environmental interactions, and embodied function in *P. stephensoni* worms. Micro-CT, biometric and tensile data reveal a clear functional differentiation between trunk and introvert, despite their shared hydrostatic coupling. The trunk exhibits high extensibility (up to ~ 100–110% strain) and moderately higher failure stresses (~ 1.6 MPa) compared to the introvert (~ 60% strain, ~ 1.0 MPa), supporting its role as a deformable pressure-generating chamber. In contrast, the introvert's reduced extensibility and conical geometry favor protrusion via unrolling at the tip rather than stretching, minimizing material strain during large elongations.

It is important to note that tensile testing performed fully submerged in seawater required the use of custom-designed miniature clamps adapted from a standard Instron setup. Although care was taken to minimize stress concentrations at the grips, occasional failures occurred at the clamping locations, reflecting an inherent limitation of the experimental configuration. Nevertheless, the majority of specimens (four out of six) failed within the central region of the samples, indicating that the reported mechanical properties are representative of the tissue behavior.

The mechanical asymmetry identified between the trunk and the introvert is essential for efficient volume redistribution. Indeed, the invariance of total body volume across functional configurations (Kruskal–Wallis, $p = 0.11$, Table 2) confirms that shape change is governed by internal pressure redistribution rather than volumetric deformation. Even small reductions in trunk radius, mediated by circular muscle contraction, produce substantial fluid displacement ($V \propto r^2$), enabling effective protrusion with limited energetic cost. This highlights how geometric amplification, rather than muscle force alone, underpins extreme elongation in sipunculans. It is important to note that, in order to perform the micro-CT scans, each specimen had to be chemically fixed in a specific configuration prior to imaging. Consequently, the measurements reported in Table 2 (unlike those in Table 1) were obtained from scans of different specimens fixed in distinct configurations, and therefore do not represent repeated measurements of the same individual in multiple states. This methodological constraint explains, for example, why the observed differences in body length (B-L) between the "Retracted" and "Partially Extended" states are attributable to natural intraspecific variability rather than to a systematic shortening during partial extension. Statistical analysis confirms that there are no significant differences between these states. The same reasoning applies to the high standard deviation of volume (V) measurements.

Beyond these mechanical aspects, the detailed morpho-anatomical analysis of *P. stephensoni* also revealed additional functional specializations. In particular, the presence of cuticular hooks or spines on the introvert (typically stiff, sclerotized epidermal structures in sipunculans, although variable in size, shape, and arrangement among species) suggests further biomechanical and ecological adaptations (Fig. 1)[54–56]. In biological systems, these relatively rigid elements contribute to substrate interaction, facilitating food collection through scraping of hard surfaces and, in some species, enhancing anchorage during burrowing or retraction. From a bioinspired perspective, analogous micro-structured features could be integrated into future soft robots to improve anchoring on rough substrates, enable directional friction control, assist in controlled attachment–detachment cycles, or enhance stability during eversion–retraction phases. Technically, such structures could be realized through multimaterial additive manufacturing to locally tailor stiffness gradients and integrate rigid micro-features within compliant bodies[57], through replica molding of elastomers against micro-patterned masters to obtain high-aspect-ratio surface protrusions[58], or by embedding stiffer micro-spine elements within a soft elastomeric matrix to create anisotropic frictional interfaces[59]. Incorporating similar fabrication approaches could allow the controlled integration of spine-like, mechanically stiffer features while preserving the overall compliance and deformability of the soft robot body. Comparable strategies have been explored in robotic systems employing microspine-based gripping mechanisms for rough surfaces and in magnetically programmable surface microstructures and artificial cilia arrays[59–62].

Indentation experiments performed on agarose-filled aquaria offer quantitative insight into the mechanical conditions encountered by the worms during confined protrusion and locomotion. Measured axial penetration forces remained relatively low (~ 0.04–0.1 N), showed only a weak dependence on penetration depth, and exhibited minimal hysteresis between loading and unloading cycles. The shallow slopes of the force–depth curves suggest that resistive forces arising from viscous drag along the body surface are minor compared to resistance associated with localized substrate yielding at the tip. This observation is consistent with a locomotion mechanism dominated by fracture or yielding of the surrounding medium rather than by continuous frictional dissipation along the body. At low penetration speeds comparable to those generated by the worms, axial forces exhibited a non-monotonic dependence on confinement, with higher forces measured in the 7 mm-wide aquarium and reduced forces in both narrower (4 mm) and wider (10 mm) channels. This trend may indicate the presence of an intermediate confinement regime in which lateral constraints are sufficient to promote effective stress build-up and force transmission at the tip, while still allowing the local deformation necessary for forward progression. By contrast, at higher penetration speeds (> 5 mm s^{-1}), measured forces exceeded 0.1 N and became largely insensitive to aquarium width, suggesting a transition toward a rate-independent or weakly viscous response of the substrate. Together, these observations support the simplified mechanical framework adopted in the peristaltic locomotion model.

The mathematical locomotion model demonstrates that effective peristaltic propulsion does not require morphological segmentation. Instead, spatially and temporally modulated strain fields, coupled with nonlinear frictional interactions, are sufficient to generate net displacement. The close agreement between simulated and experimental trajectories, both in cumulative displacement and temporal evolution, confirms that continuous bodies can exploit differential friction and internal strain waves to achieve locomotion at characteristic speeds of ~ 0.5–5 mm/s. This challenges the prevailing paradigm that segmentation is a prerequisite for efficient peristalsis and highlights a viable alternative design strategy for innovative soft robotic systems based on fully continuous architectures[27,63,64]. Indeed, only a few robotic examples in this direction have been reported in the literature[65,66] and none currently combine both eversion and peristaltic locomotion within a single continuous soft structure, as observed in unsegmented worms.

Our findings suggest that peristaltic locomotion does not inherently require segmentation, but rather relies on the coordinated action of circular and longitudinal muscle layers. Moreover, in sipunculan worms, circular muscles are also actively involved in introvert protrusion, revealing a multifunctional muscular organization that provides an even more compelling biological model for the development of bio-inspired soft robotic systems. This functional versatility is enabled by the distinct morphological differentiation between the introvert and the trunk with the trunk primarily acting as a propulsive unit, while the structure of the introvert facilitates distal eversion and forward elongation. Introvert protrusion kinematics further clarify how these structural and environmental factors translate into functional performance during burrowing. Quantitative analyses showed that both protrusion and retraction speeds depend on the degree of lateral confinement imposed by the substrate. The highest velocities were consistently measured in the 7 mm-wide aquaria (protrusion: 1.13 ± 0.39 mm s^{-1}; retraction: 1.79 ± 0.82 mm s^{-1}), whereas reduced speeds were observed under both stronger (4 mm) and weaker (10 mm) confinement. These observations may be interpreted in light of the mechanical response of the gel: at low penetration speeds comparable to those generated by the worms, intermediate confinement appears to favor more effective stress localization and axial force transmission at the tip, while still permitting the local substrate deformation required for forward advancement. By contrast, narrower channels may limit gel rearrangement during eversion, whereas wider channels may allow deformation modes that dissipate energy laterally, resulting in less efficient burrowing. Importantly, protrusion speed showed no clear scaling with body size, indicating that introvert eversion is primarily governed by local hydrostatic pressure redistribution and tip–substrate interactions rather than by overall body dimensions.

The proposed soft robotic prototype illustrates how the biological principles identified in *P. stephensoni* can be embodied in an engineered system without centralized control or rigid actuation. By combining ultra-soft trunk structure (Ecoflex 00–10) with stiffer magnetically responsive artificial muscles (DragonSkin-10 loaded with 70 wt% NdFeB particles) and stiffer introvert (DragonSkin-10), the robot reproduces hydraulic protrusion through material-mediated interactions. From a mechanical perspective, the design and material selection were not intended to match absolute stress–strain values, but rather to reproduce the functional stiffness hierarchy and nonlinear response observed in the biological tissues (Figs. 6 and 15). In monotonic tests at break, the introvert tissue exhibits a steep stress–strain response, reaching approximately 1–1.5 MPa at strains below ~ 1. DragonSkin-10 attains comparable stress levels at higher strains (approximately 2–3), reaching about 2 MPa at strain of ~ 3.5. Conversely, trunk tissue develops substantially lower stresses at small-to-moderate strains, followed by progressive stiffening at larger deformations. Within strains below 0.4, EcoFlex 00–10 exhibits stress levels on the order of tens of kPa, consistent with those measured in trunk tissue within the same deformation range. However, EcoFlex 00–10 remains below 1 MPa even at very large strains (> 6), whereas the biological trunk tissue exceeds 1 MPa at strains between 0.8 and 1.2. This difference is mitigated by the presence of embedded magnetically responsive regions made of DragonSkin-10 loaded with 70 wt% NdFeB particles, which locally increase the effective stiffness of the trunk structure.

Cyclic tests further support a clear quantitative difference in mechanical response between the two selected silicones: at strain of ~ 2, DragonSkin-10 develops stresses close to 900 kPa, whereas EcoFlex 00–10 remains below ~ 80 kPa, confirming the pronounced stiffness contrast between the two materials. Thus, although some differences between the mechanical properties of the worm tissues and the selected silicones are inevitably present, the primary design criterion (namely, achieving a clear relative contrast in stiffness and compliance, as observed in the worm tissues) was successfully satisfied, resulting in a mechanically differentiated system composed of a stiffer, deformation-guiding introvert and a highly compliant, hydrostatically active trunk.

The measured elongation ratio of the final soft robot, equal to 2.5 times its initial length, falls within the biological range and demonstrates an efficient strategy for achieving large elongations through wireless magnetic actuation, reaching elongation levels that are rarely reported among existing magnetically driven soft robotic designs in the literature. Indeed, by exploiting a magneto-fluidic transmission mechanism, the proposed design achieves displacements of up to 45 mm, i.e. roughly 9× greater than the ~ 5 mm reported for previous similarly sized devices that rely on direct magnetic actuation[25]. Other solutions have demonstrated stiffness-variable photothermal magnetic composites that achieve axial strains approaching ~ 400% at the device level and stretchability exceeding 800% at the material level[67]. However, such systems rely on direct gradient magnetic forces to pull a highly compliant structure toward a magnetic source. In contrast, our approach is torque-driven and converts magnetic actuation into fluid transmission, enabling protrusion of a passive soft proboscis structure through hydrostatic pressure redistribution. This avoids direct magnetic attraction toward the field source and the associated nonlinear force amplification, which may introduce stability and controllability challenges in gradient-based pulling configurations.

Crucially, actuation arises from magnetic torque generated by programmed magnetization profiles, which induce bending of trunk regions and thereby produce trunk compression and internal fluid displacement, all without the need for embedded electronics or pneumatic lines. Passive elastic elements replicate retractor muscle function, ensuring rapid and reliable retraction. By capturing the core physical mechanisms underlying hydrostatically driven protrusion, this prototype highlights the potential of biologically grounded design principles to guide future soft robotic architectures. Additionally, the proposed system should also be interpreted within the broader framework of bioinspired robotics as a methodological tool for biological understanding.

While bioinspired robotics is often employed to translate natural strategies into engineered solutions, it also plays a complementary role by providing simplified, controllable physical models that help isolate and analyze the fundamental principles governing biological systems. In this perspective, the present architecture offers a biologically and functionally grounded model for the study of hydrostatic skeletons, as well as for gaining insight into a group of worms that remains relatively understudied and still debated within the field of biology.

In addition to its relevance as a research tool, the proposed architecture may offer a potential pathway toward implementation as a fully soft, wirelessly actuated pumping or valving module, for example for use in sealed and sterile environments. In bioprocessing, single-use bioreactors, or closed fluidic systems, mechanical feedthroughs and pneumatic connections often represent critical sources of leakage and contamination. In this context, the present design could, in principle, enable actuation across sealed boundaries without physical interfaces, as magnetic fields can penetrate non-magnetic walls and induce controlled internal fluid displacement. By leveraging its pressure-generation capability and linear motion, the system may function as a compact dosing unit, a low-frequency pulsatile pump, or a soft valve entirely enclosed within a sterile chamber, thereby reducing reliance on external tubing and minimizing contamination risks. Nevertheless, its current applicability remains limited by centimeter-scale dimensions and relatively low actuation bandwidth, and further studies are required to explore miniaturization and performance optimization. Moreover, precise flow-rate regulation would likely require the integration of additional passive or active flow-control elements, such as soft valves. Despite these constraints, this architecture establishes a promising proof-of-concept for wireless fluid actuation in closed environments, highlighting its dual potential as both a research platform and a prospective engineering strategy for controlled fluid handling in sealed systems.

Methods

The model organism

The sipunculan *Phascolosoma stephensoni* (Stephen, 1942) was originally described from South Africa (Stephen, 1942), but subsequently reported from several localities in temperate and warm waters, including the Mediterranean Sea[68]. The identity of this species has been the subject of considerable nomenclatural and taxonomic debate[69], as several nominal species described in the second half of the 20th century were synonymized with it[68], while it was also historically misidentified as *Phascolosoma granulatum* Leuckart, 1828, i.e., a species originally described from the North Sea, but until recently considered widespread in the Mediterranean Sea[68,70]. Recent evidence suggests that, even though published reports of *P. stephensoni* are still scattered, the species occurring with abundant populations in hard substrates on shallow environments of the Mediterranean Sea is indeed *P. stephensoni*[71,72]. A similar confusion accounts for genetic data, as sequences clearly belonging to the same species deposited in public repositories are assigned to both *P. granulatum* and *P. stephensoni*[26]. *Phascolosoma stephensoni*is typically associated with hard substrates from the intertidal zone to > 1000 m depth, where it is seemingly able to actively burrow in the rock, even though the mechanism employed is currently unknown[68]. It is typically the most abundant sipunculan in intertidal assemblages dominated by articulate coralline algae, but it can also be found in deeper coralligenous outcrops structured by crustose coralline algae, and in association with sponges[10,68]. In natural conditions, individuals of *P. stephensoni* settle in crevices and burrows in the hard substrate, bending their trunk to interlock with irregularities of the rock surface. Reproduction in *P. stephensoni* in the Mediterranean Sea is currently scarcely known, but all *Phascolosoma* species studied up to now are characterized by the presence of long planktonic larval stages, allowing for a wide dispersal range. Gametogenic cycle and larval development were studied in the closely related *Phascolosoma agassizii* (Keferstein, 1866) in several localities in the Pacific Ocean, where spawning was reported either in summer[73,74] or in early spring[75], suggesting either a wide reproductive plasticity, or the possible occurrence of different species identified with the same name. In Mediterranean specimens employed in this study, ripe gametes were found between October and December, suggesting the possibility of spawning occurring in Winter.

We chose *P. stephensoni* as the model species for this study, considering both its high frequency and abundance in shallow-water environments, which facilitate sampling, and its adaptation to intertidal life, which confers tolerance to variations in environmental conditions such as salinity and temperature, thereby resistant under rearing conditions. Moreover, previous studies suggested that *P. stephensoni*might represent an interesting and suitable model for bioinspiration[10].

Animal collection and experimental settings

Individuals of *P. stephensoni* were sampled in intertidal environments along the coast of Salento (Southeast Italy) and maintained in an aquarium filled with filtered seawater at 23 °C. Aquaria were fitted with clean, smooth pebbles with an average diameter of 5 cm to reduce the stress on the worms by allowing them to take shelter. Worms were fed every 20 days with a mix of spirulina, dead *Artemia salina* and coralline algae to mimic the organic debris occurring in the marine environment. Oxygenation was maintained through an aerator, and the seawater in the aquarium was changed every month. Individuals lasted in the aquarium for more than one year since the harvesting at sea (when they were already adult specimens), suggesting a lifespan potentially exceeding two years and highlighting the suitability of the aquarium setting for the rearing of this species.

Standardized measurements of external anatomy were performed on live individuals of *P. stephensoni* placed in three narrow, custom-built experimental aquaria (100×100 mm^2) with widths of 4 mm, 7 mm, and 10 mm for small, medium, and large worms, respectively, and filled with a 0.5% agarose gel prepared in filtered seawater (Fig. 7). The reduced lateral dimensions of the aquaria constrained the worms' movement to approximately two dimensions, thereby simplifying the extraction of shape and locomotion data from video frames.

High-resolution video recordings of worms were acquired at 50 fps. A high-resolution digital camera (Canon EOS 90D) positioned in front of the aquaria and a calibrated 10 mm grid placed in the background were used to enable precise morphological quantification. Specifically, sequential frames corresponding to the fully retracted and fully extended states were extracted and analyzed using the *ImageJ* software. Measurements of body length and diameter (at equidistant points along the worm's body) were taken on ten different individuals, under each experimental condition.

For the characterization of peristaltic locomotion, tail positions were tracked using the open-source software Tracker (version 6.1.5, Open Source Physics), allowing precise extraction of displacement–time profiles. In addition, protrusion and retraction speeds of the introvert within the gel-filled aquaria were quantified by tracking its displacement across consecutive frames using ImageJ, based on known time intervals. For each individual and experimental condition, at least five independent speed measurements were obtained.

The agarose gel was prepared by mixing agarose powder (Agarose Type I, low EEO, Sigma-Aldrich) with salty water (3.8 g/L of sodium chloride) under continuous stirring at 90 °C. Maintaining the controlled temperature ensured proper dissolution and homogenization. The mixture was then left cooling until it reached 50 °C, poured into the custom-built aquaria and allowed to cool to room temperature until gelation was complete.

The mechanical properties of the 0.5 wt% agarose gel in the same aquaria used for worm experiments were characterized through indentation tests using a uniaxial testing machine (Instron 5695, Instron) equipped with a 10 N load cell. These tests quantified the mechanical properties of the environment in which the worms were moving. To simulate the worm, a metallic rod with a diameter comparable to that of the worm's introvert (3 mm) was connected to the load cell and used as an indenter to record the axial force exerted during penetration. As in the worm experiments, the aquaria had three width values ($w = 4$ mm, 7 mm, and 10 mm), while two combinations of height (h) and length (l) were tested, namely $l = h = 50$ mm and $l = h = 100$ mm, in order to investigate the influence of confinement and available penetration distance on the measured mechanical response of the gel (Fig. 7). In the former case, the penetration length was fixed at 30 mm, whereas in the latter it was set to 55 mm. Penetration tests were conducted at four speeds ($v = 0.5$, 1, 5, and 10 mm/s). Each condition was tested five times at different locations within the gel to assess potential boundary effects, and the resulting force values were averaged.

Micro-CT scanning and analysis

Thirteen specimens of *P. stephensoni* in three body configurations (retracted, partially extended, and fully extended) were anesthetized using either an isotonic solution of magnesium chloride ($MgCl_2$) in distilled water, or a thymol–seawater solution, and then fixed in 10% buffered formalin prepared in filtered seawater. Subsequently, the specimens were washed with distilled water to remove residual formalin and dehydrated in a graded ethanol series up to 96% ethanol. Specimens were stained with 1% iodine (I_2) dissolved in 96% ethanol (modified staining protocol included in Metscher et al.[76] as a contrast-enhancing agent to improve visualization of internal anatomical structures).

Micro-CT was used to visualize the internal morphological structures, with particular emphasis on the musculature responsible for introvert dynamics. This imaging technique is a high-resolution, non-destructive imaging technique that employs X-rays to acquire detailed cross-sectional projections of small-scale specimens. In this study, micro-CT scans were performed using a SkyScan 1172 microtomograph (Bruker, Kontich, Belgium) at the Hellenic Centre for Marine Research (HCMR). Sipunculan specimens were scanned at 60 kV and 167 μA, without filter, for a full rotation of 360°. Images were acquired at a pixel size of approximately 4.8 μm with a camera binning of 1 × 1. The exposure time was 318 ms, with frame averaging set to 3. Projection images were reconstructed into cross-sectional images using SkyScan's NRecon v.1.7.4.2 software (Bruker, Kontich, Belgium) with attenuation coefficients in the range of 0–0.29. Volume renderings of each specimen were generated using CTVox software (Bruker, Kontich, Belgium). Additional details about the microCT protocols are reported in Keklikoglou et al.[77].

For 2D morphometric analysis, cross-sectional images were loaded into DataViewer v.1.6.5.2 software (Bruker, Kontich, Belgium) to measure the total body length and the length of the four retractor muscles. 3D analyses were performed using CTAn v.1.18.4.0 software (Bruker, Kontich, Beligum), allowing the computation of total body volume and retractor muscle thickness. Volume renderings of sipunculan specimens were created using the CTVox v.3.3.1 software (Bruker, Kontich, Belgium).

Since the assumptions of parametric ANOVA were violated, non-parametric Kruskal-Wallis tests[78] were applied to assess differences in body length, retractor muscle length, body volume, and retractor muscle thickness across the three body configurations. Dunn's test[79] with Bonferroni correction, was used for post hoc comparisons. All analysis were conducted in R (version 4.4.1)[80] using the rstatix package (version 0.7.2)[81].

Biomechanical properties of soft tissues

Uniaxial tensile tests on trunk and introvert samples were conducted at a constant elongation rate of 1 mm/s, using a Universal Testing machine (Instron 5965, USA) equipped with a 10 N load cell at The BioRobotics Institute and Department of Excellence in Robotics & AI, Sant'Anna School of Advanced Studies. Following dissection, each body part was carefully mounted and secured using custom-designed clamps. The specimens were tested in filtered seawater within an aquarium setup to preserve physiological hydration and ionic conditions, thereby minimizing dehydration-induced artifacts in tissue mechanics and ensuring that the measured responses were representative of in vivo-like behavior. Both cyclic tensile tests (consisting of 50 cycles of uniaxial extension up to 10% strain for the introvert and up to 70% strain for the trunk) and monotonic tensile tests to failure were performed to characterize the mechanical response and ultimate performance of the tissues. To minimize preconditioning effects, the first 10 cycles of cyclic tests were discarded from the analysis, and only the subsequent 40 cycles were considered for the final evaluation.

To quantitatively describe the nonlinear elastic behavior observed in the stress–strain responses, the Ogden hyperelastic model was subsequently employed, as it is well suited for capturing large deformations typical of soft biological tissues. Assuming a uniaxial stress condition, the model formulation is based on the principal Cauchy stress expression, which depends on the stretch λ (λ = + 1 where the strain = $\frac{\Delta l}{l_0}$) and on the material parameters μ_p and α_p. Specifically, the engineering stress–stretch relationship is defined as[82,83]:

$$\sigma = \sum\nolimits_{p=1}^{N} \mu_p (\lambda^{\alpha_p - 1} - \lambda^{-\left(\frac{\alpha_p + 2}{2}\right)})$$

A MATLAB-based fitting script was developed to extract the material parameters of the Ogden hyperelastic model ($N = 3$). The quality of the fit was quantified by calculating the coefficient of determination (R^2) for each sample. The custom-developed script is provided in the Supplementary Materials. Specifically, the script performs a nonlinear least-squares optimization using MATLAB's *lsqcurvefit* function to minimize the difference between the experimental stress–strain data and the model prediction. Parameter bounds are imposed to ensure physically meaningful values of μ_p and α_p, and convergence is controlled through predefined tolerances and iteration limits.

Magnetically-driven soft robots manufacturing and testing

The worm-inspired robot was fabricated through a multi-step soft-molding process designed to integrate magnetically active and passive components into a single, fully compliant structure. First, the four magnetically responsive bending elements were fabricated using dedicated silicone molds. Each actuator was cast from a composite elastomer consisting of DragonSkin-10 (Smooth-On Inc., USA), prepared by mixing Part A and Part B in a 1:1 weight ratio and loading the mixture with hard magnetic NdFeB microparticles (MQP-B+, Magnequench GmbH, Germany). The composite was degassed under vacuum to remove trapped air and cured at room temperature, yielding flexible magnetic actuators with uniform particle distribution. The trunk was then fabricated as a hollow, fluid-tight body using a separate silicone mold. Prior to casting, the four magnetic bending elements were symmetrically positioned inside the mold to ensure correct alignment along the trunk walls. The mold was subsequently filled with Ecoflex™ 00–10 (Smooth-On Inc., USA), mixed at a 1:1 ratio by weight, and degassed before casting. After curing, this process resulted in a compliant trunk with embedded magnetic actuators mechanically integrated within the surrounding elastomeric matrix. To enhance structural stability and limit excessive deformation at the base during magnetic actuation, the bottom portion of the trunk was locally reinforced by casting an additional layer of stiffer silicone (Smooth-Sil™ 960, Smooth-On Inc., USA).

The proboscis was manufactured separately as a thin-walled, conical structure using dip-coating as the primary and only fabrication method. A higher Shore hardness silicone (DragonSkin-10, Smooth-On Inc., USA), diluted with silicone thinner (Silicone Thinner™, Smooth-On Inc., USA) to reduce viscosity, was employed to achieve a uniform wall thickness on the order of a few hundred micrometers and provide greater resistance to radial expansion compared to the softer silicone used for the trunk. This approach was selected to reproduce the reduced extensibility and unrolling-dominated eversion behavior observed in the biological introvert. Indeed, mechanical characterization of P. stephensoni tissues revealed that the introvert exhibits lower extensibility than the trunk and protrudes primarily through geometric unrolling rather than stretching. The 3D-printed mold with the desired conical geometry was immersed in diluted DragonSkin-10 and the coated mold was then cured in an inverted configuration, with the tip of the cone oriented downward for approximately 4 h. This orientation allowed gravity-driven flow to further reduce and homogenize wall thickness. The resulting silicone layer had a thickness of approximately 200 μm, which would not have been achievable through conventional molding techniques, and wall thickness plays a critical role in proboscis performance. Because bending stiffness scales with the cube of thickness, even modest increases in wall thickness would significantly increase structural stiffness, require higher internal pressure to initiate eversion, and reduce unrolling efficiency. Minimizing thickness therefore enables geometric eversion at lower pressure while maintaining sufficient circumferential stiffness to limit parasitic radial expansion. The use of a stiffer silicone combined with a thin-walled geometry ensures that, during actuation, internal fluid displacement drives axial eversion rather than radial stretching, thereby improving stroke efficiency and output force without the need for additional fiber reinforcements or strain-limiting elements. After curing, the proboscis was mechanically coupled to the trunk using silicone glue (Sil-Poxy™, Smooth-On Inc., USA).

Passive elastic strips acting as artificial retractor elements were then attached between the base of the trunk and the distal region of the proboscis. These elements were fabricated from an ultra-soft silicone (Ecoflex™ 00–10, Smooth-On Inc., USA) by casting thin sheets using a film applicator, followed by cutting into narrow strips using a surgical scalpel. The dimensions of the strips were selected to provide adequate restoring force for retraction without significantly hindering protrusion.

Finally, the assembled structure was sealed using silicone glue, filled with a controlled volume of deionized water serving as the internal working fluid, and hermetically closed.

The soft robot was actuated using an N35-grade diametrically magnetized cylindrical external permanent magnet (EPM) (outer diameter = 60 mm, inner diameter = 10 mm, length = 70 mm). The magnet was mounted on a robotic arm, which allowed precise control and modulation of the distance between the magnet and the bottom surface of the soft robot (see also Figure S3 in the Supplementary Materials). This configuration provided a strong and spatially extended magnetic field suitable for the effective actuation of the embedded magnetic particles within the worm-inspired soft robot. The magnetic field intensity was adjusted by varying the magnet–robot distance from a maximum of approximately 95 mm (~ 10 mT), corresponding to the fully retracted proboscis configuration, to a minimum of approximately 5 mm (~ 250 mT), corresponding to the fully extended proboscis configuration. The magnetic field intensity was measured using a 3-axis magnetic sensor hall-effect (TLE493D-W2B6, Infineon).

FEM simulations of magnetic benders

To investigate the mechanics of the magnetically actuated bending units embedded in the soft robot trunk, we developed a finite element (FEM) model implemented in the equation-based module of COMSOL Multiphysics. The magnetic bender was modelled as a composite strip made of DragoSkin-10 silicone loaded with 70%wt NdFeB particles. Owing to geometric symmetry, only half of the magnetic bending layer was simulated. The layer was clamped at one edge to reproduce a cantilever boundary condition, while all remaining surfaces were free. The magnetic dipoles were assumed to remain perpendicular to the local tangent vector along the strip centerline. The mechanical behavior of the magnetic elastomer was described using the Ogden hyperelastic model, with parameters obtained from tensile tests performed on DragonSkin-10 containing 70 wt% NdFeB particles (Table S5). Gravitational effects were neglected and a uniform external magnetic field up to 50 mT was applied along the Z axis.

Data availability

The codes and datasets generated in this study are available through the MAPWORMS Community on Zenodo (https://zenodo.org/communities/mapworms) or from the corresponding author upon reasonable request.

Received: 19 January 2026; Accepted: 9 March 2026

References

1. Ellers, O. et al. Soft skeletons transmit force with variable gearing. *J. Exp. Biol.* **227** (2024).
2. Kier, W. M. The diversity of hydrostatic skeletons. *J. Exp. Biol.* **215**, 1247–1257 (2012).
3. Chubb, K. et al. Soft robots and soft bodies: Biological insights into the structure and function of fluidic soft robots. *Bioinspir. Biomim.* **20**, 013001 (2024).
4. Pfeifer, R., Lungarella, M. & Iida, F. Self-organization, embodiment, and biologically inspired robotics. *Science* **318**, 1088–1093 (2007).
5. Laschi, C. & Mazzolai, B. Lessons from animals and plants: The symbiosis of morphological computation and soft robotics. *IEEE Robot. Autom. Mag.* **23**, 107–114 (2016).
6. Sitti, M. Physical intelligence as a new paradigm. *Extreme Mech. Lett.* **46**, 101340 (2021).
7. Jin, Y., Li, J., Liu, S., Cao, G. & Liu, J. A worm-inspired robot based on origami structures driven by the magnetic field. *Bioinspir. Biomim.* **18**, 046008 (2023).
8. Zhao, Y., Huang, H., Yuan, W., Liu, X. & Cao, C. C. Worm-inspired, untethered, soft crawling robots for pipe inspections. *Soft Robot.* **11**, 639–649 (2024).
9. Liu, X., Song, M., Fang, Y., Zhao, Y. & Cao, C. Worm-inspired soft robots enable adaptable pipeline and tunnel inspection. *Adv. Intell. Syst.* **4**, 2100128 (2022).
10. Filogna, S., Iacovacci, V., Vecchi, F., Musco, L. & Menciassi, A. Protrusion mechanism study in sipunculid worms as model for developing bio-inspired linear actuators. *Bioinspir. Biomim.* **16**, 026008 (2020).
11. Weigert, A. & Bleidorn, C. Current status of annelid phylogeny. *Org. Divers. Evol.* **16**, 345–362 (2016).
12. Struck, T. H. et al. Phylogenomic analyses unravel annelid evolution. *Nature* **471**, 95–98 (2011).
13. Huang, D. Y., Chen, J. Y., Vannier, J. & Salinas, J. I. S. Early Cambrian sipunculan worms from southwest China.. *Proc. R. Soc. Lond. B Biol. Sci.* **271**, 1671–1676 (2004).
14. Schulze, A., Boyle, M. J., Kawauchi, G. Y., Kerbl, A. & Worsaae, K. 6. Amphinomida/Sipuncula. In *Annelida* 177–216 (2019). https://doi.org/10.1515/9783110291582-006.
15. Langeneck, J. et al. Bridging past and present: The Salento Peninsula as a case study for unveiling marine annelid diversity by integrating literature, field surveys, and DNA barcoding. *Eur. Zool. J.* **93**, 270–297 (2026).
16. Schulze, A. & Kawauchi, G. Y. How many sipunculan species are hiding in our oceans?. *Diversity* **13**, 43 (2021).
17. Schulze, A. & Rice, M. E. Musculature in sipunculan worms: Ontogeny and ancestral states. *Evol. Dev.* **11**, 97–108 (2009).
18. Hawkes, E. W., Blumenschein, L. H., Greer, J. D. & Okamura, A. M. A soft robot that navigates its environment through growth.. *Sci. Robot.* https://doi.org/10.1126/scirobotics.aan3028 (2017).
19. Coad, M. M. et al. Vine robots: Design, teleoperation, and deployment for navigation and exploration. *IEEE Robot Autom. Mag* **27**, 120–132 (2020).
20. Filogna, S. et al. A bioinspired fluid-filled soft linear actuator. *Soft Robot* **10** (2023).
21. Urban, M. W. Stimuli-Responsive Materials: From Molecules to Nature Mimicking Materials Design. In *Stimuli-Responsive Materials: From Molecules to Nature Mimicking Materials Design*. https://doi.org/10.1039/9781839169045 (2016).
22. Chung, H.-J., Parsons, A. M. & Zheng, L. Magnetically controlled soft robotics utilizing elastomers and gels in actuation: A review. *Adv. Intell. Syst.* **3**, 2000186 (2021).
23. Kim, Y. & Zhao, X. Magnetic soft materials and robots. *Chem. Rev.* **122**, 5317–5364 (2022).
24. Dong, Y. et al. Untethered small-scale magnetic soft robot with programmable magnetization and integrated multifunctional modules. *Sci. Adv.* **8**, 8932 (2022).
25. Lin, D., Yang, F., Gong, D. & Li, R. Bio-inspired magnetic-driven folded diaphragm for biomimetic robot. *Nat. Commun.* **14**, 163 (2023).
26. Langeneck, J. et al. Bridging past and present: the Salento Peninsula as a case study for unveiling marine anneliddiversity by integrating literature, fi eld surveys, and DNA barcoding. *Eur. Zool. J.* **93**, 270–297 (2026).
27. Agostinelli, D., Alouges, F. & DeSimone, A. Peristaltic waves as optimal gaits in metameric bio-inspired robots. *Front. Robot. AI* **5**, 385739 (2018).
28. DeSimone, A., Guarnieri, F., Noselli, G. & Tatone, A. Crawlers in viscous environments: Linear vs non-linear rheology. *Int. J. Non-Linear Mech.* **56**, 142–147 (2013).
29. Norouzikudiani, R., Lucantonio, A. & DeSimone, A. Equilibrium and transient response of photo-actuated liquid crystal elastomer beams. *Mech. Res. Comm* **131**, 104126 (2023).
30. Kim, S., Laschi, C. & Trimmer, B. Soft robotics: A bioinspired evolution in robotics. *Trends Biotechnol.* **31**, 287–294 (2013).
31. Kurth, J. A. & Kier, W. M. Scaling of the hydrostatic skeleton in the earthworm *Lumbricus terrestris*. *J. Exp. Biol.* **217**, 1860–1867 (2014).
32. Herranz, M., Boyle, M. J., Pardos, F. & Neves, R. C. Comparative myoanatomy of Echinoderes (Kinorhyncha): a comprehensive investigation by CLSM and 3D reconstruction. *Front. Zool.* **11** (1), 11–31 (2014). 2014.
33. Grill, S. & Dorgan, K. M. Burrowing by small polychaetes - Mechanics, behavior and muscle structure of *Capitella* sp. *J. Exp. Biol.* **218**, 1527–1537 (2015).

34. Lin, H. T., Slate, D. J., Paetsch, C. R., Dorfmann, A. L. & Trimmer, B. A. Scaling of caterpillar body properties and its biomechanical implications for the use of a hydrostatic skeleton. *J. Exp. Biol.* **214**, 1194–1204 (2011).
35. Berni, J., Pulver, S. R., Griffith, L. C. & Bate, M. Autonomous circuitry for substrate exploration in freely moving *Drosophila* larvae. *Curr. Biol.* **22**, 1861–1870 (2012).
36. Kier, W. M. & Stella, M. P. The arrangement and function of octopus arm musculature and connective tissue. *J. Morphol.* **268**, 831–843 (2007).
37. Di Clemente, A., Maiole, F., Bornia, I. & Zullo, L. Beyond muscles: Role of intramuscular connective tissue elasticity and passive stiffness in octopus arm muscle function.. *J. Exp. Biol.* https://doi.org/10.1242/jeb.242644 (2021).
38. Zhao, Y., Huang, H., Yuan, W., Liu, X. & Cao, C. C. Worm-inspired, untethered, soft crawling robots for pipe inspections. *Soft Robot.* **11**, 639–649 (2024).
39. Liu, X., Song, M., Fang, Y., Zhao, Y. & Cao, C. Worm-inspired soft robots enable adaptable pipeline and tunnel inspection. *Adv. Intell. Syst.* **4**, 2100128 (2022).
40. Muff, L. F. et al. Modular design of a polymer-bilayer-based mechanically compliant worm-like robot. *Adv. Mater.* **35**, 2210409 (2023).
41. Jin, Y., Li, J., Liu, S., Cao, G. & Liu, J. A worm-inspired robot based on origami structures driven by the magnetic field. *Bioinspir. Biomim.* **18**, 046008 (2023).
42. Pan, M. et al. Bioinspired mechanisms and actuation of soft robotic crawlers. *Adv. Sci.* **12**, 2416764 (2025).
43. Wu, S., Hong, Y., Zhao, Y., Yin, J. & Zhu, Y. Caterpillar-inspired soft crawling robot with distributed programmable thermal actuation.. *Sci. Adv.* https://doi.org/10.1126/sciadv.adf8014 (2023).
44. Xie, Z. et al. Octopus-inspired sensorized soft arm for environmental interaction. *Sci. Robot.* **8**, 7852 (2023).
45. Yue, T. et al. Embodying soft robots with octopus-inspired hierarchical suction intelligence.. *Sci. Robot.* https://doi.org/10.1126/scirobotics.adr4264 (2025).
46. Jiang, P. et al. An octopus-inspired soft pneumatic robotic arm. *Biomimetics* **9**, 773 (2024).
47. Sozer, C., Sahu, S. K., Paterno, L. & Menciassi, A. Robotic modules for a continuum manipulator with variable stiffness joints. *IEEE Robot. Autom. Lett.* **8**, 4745–4752 (2023).
48. Das, R., Babu, S. P. M., Visentin, F., Palagi, S. & Mazzolai, B. An earthworm-like modular soft robot for locomotion in multi-terrain environments. *Sci. Rep.* **13**, 1571 (2023).
49. Riddle, S. A., Jackson, C. B., Daltorio, K. A. & Quinn, R. D. A 3D model predicts behavior of a soft bodied worm robot performing peristaltic locomotion. *Bioinspir. Biomim.* **20**, 066001 (2025).
50. Xu, L. et al. Locomotion of an untethered, worm-inspired soft robot driven by a shape-memory alloy skeleton. *Sci. Rep.* **12**, 12392 (2022).
51. Jing, Z., Li, Q., Su, W. & Chen, Y. Dielectric elastomer-driven bionic inchworm soft robot realizes forward and backward movement and jump. *Actuators* **11**, 227 (2022).
52. Jin, Y., Li, J., Liu, S., Cao, G. & Liu, J. A worm-inspired robot based on origami structures driven by the magnetic field. *Bioinspir. Biomim.* **18**, 046008 (2023).
53. Hawkes, E. W., Blumenschein, L. H., Greer, J. D. & Okamura, A. M. A soft robot that navigates its environment through growth. *Sci. Robot.* **2**, 3028 (2017).
54. Anderson, D. T. Polychaetes and allies: The southern synthesis. Fauna of Australia. Vol 4a. Polychaeta, Myzostomida, Pogonophora, Echiura, Sipuncula.
55. Cutler, E. B. The Sipuncula : Their Systematics, Biology, and Evolution. (2018). https://books.google.com/books/about/The_Sipuncula.html?id=vSVzDwAAQBAJ
56. Rice, M. Sipunculans Associated with Coral Communities 1.
57. Raj, R., Song, Q. & Juang, J. Multi-material additive manufacturing of soft robotic systems: A comprehensive review. *Adv. Rob. Res.* https://doi.org/10.1002/adrr.202500064 (2025).
58. del Campo, A. & Arzt, E. Fabrication approaches for generating complex micro- and nanopatterns on polymeric surfaces. *Chem. Rev.* **108**, 911–945 (2008).
59. Asbeck, A. T., Kim, S., Cutkosky, M. R., Provancher, W. R. & Lanzetta, M. Scaling hard vertical surfaces with compliant microspine arrays. *Int. J. Robot. Res.* **25**, 1165–1179 (2006).
60. Zhang, S. et al. 3D-printed micrometer-scale wireless magnetic cilia with metachronal programmability. *Sci. Adv.* https://doi.org/10.1126/sciadv.adf9462 (2023).
61. Li, X. et al. An underactuated adaptive microspines gripper for rough wall. *Biomimetics* **8**, 39 (2023).
62. Gu, H. et al. Magnetic cilia carpets with programmable metachronal waves. *Nat. Commun.* **11**, 2637 (2020).
63. Tanaka, Y., Ito, K., Nakagaki, T. & Kobayashi, R. Mechanics of peristaltic locomotion and role of anchoring. *J. R Soc. Interface.* **9**, 222–233 (2012).
64. Glenn, K. Kinematic scaling of locomotion by hydrostatic animals. *J. Exp. Biol.* **202**, 661–674 (1999).
65. Sharma, S. et al. Wireless peristaltic pump for transporting viscous fluids and solid cargos in confined spaces. *Adv. Funct. Mater.* **34**, 2405865 (2024).
66. Zhang, J. et al. Voxelated three-dimensional miniature magnetic soft machines via multimaterial heterogeneous assembly. *Sci. Robot.* https://doi.org/10.1126/scirobotics.abf0112 (2021).
67. Seong, M. et al. Multifunctional magnetic muscles for soft robotics. *Nat. Commun.* https://doi.org/10.1038/s41467-024-52347-w (2024).
68. Murina, G. V. V., Pancucci-Papadopoulou, M. A. & Zenetos, A. The phylum Sipuncula in the Eastern Mediterranean: Composition, ecology, zoogeography. *J. Mar. Biol. Assoc. U. K.* **79**, 821–830 (1999).
69. Cutler, E. B. The Sipuncula : Their Systematics, Biology, and Evolution. (2018). https://books.google.com/books/about/The_Sipuncula.html?id=vSVzDwAAQBAJ
70. Zool, T. J. & Açik, Ş. Checklist of Sipuncula from the coasts of Turkey. *Turk. J. Zool.* **38**, 723–733 (2014).
71. Ferrero-Vicente, L., Rubio-Portillo, E. & Ramos-Espla, A. Sipuncula inhabiting the coral *Oculina patagonica* in the Western Mediterranean Sea. *Mar. Biodivers. Rec.* **9**, 1–7 (2016).
72. Açik, S. Sipunculan fauna in the Fethiye-Gφηek Specially Protected Area (Turkey, Eastern Mediterranean). *Mediterr. Mar. Sci.* **11**, 105–116 (2010).
73. Rice, M. E. A comparative study of the development of *Phascolosoma agassizii*, *Golfingia pugettensis*, and *Themiste pyroides* with a discussion of developmental patterns in the Sipuncula. *Ophelia* **4**, 143–171 (1967).
74. Adrianov, A. V., Maiorova, A. S. & Malakhov, V. V. Embryonic and larval development of the peanut worm *Phascolosoma agassizii* (Keferstein 1867) from the Sea of Japan (Sipuncula: Phascolosomatidea). *Invertebr. Reprod. Dev.* **55**, 22–29 (2011).
75. Towle, A. & Giese, A. C. The annual reproductive cycle of the sipunculid *Phascolosoma agassizii*. *Physiol. Zool.* **40**, 229–237. https://doi.org/10.1086/physzool.40.3.30152860 (1967).
76. Metscher, B. D. Micro CT for comparative morphology: Simple staining methods allow high-contrast 3D imaging of diverse non-mineralized animal tissues. *BMC Physiol.* **9**, 1–14 (2009).
77. Keklikoglou, K., Langeneck, J. & Musco, L. MAPWORMS Micro-CT imaging protocols. https://doi.org/10.5281/ZENODO.14039803 doi:10.5281/ZENODO.14039803.
78. Kruskal, W. H. & Wallis, W. A. Use of ranks in one-criterion variance analysis. *J. Am. Stat. Assoc.* **47**, 583–621 (1952).
79. Dunn, O. J. Multiple comparisons using rank sums. *Technometrics* **6**, 241–252 (1964).

80. org/, R. C. T. R. & undefined. R: A language and environment for statistical computing. R Foundation for Statistical Computing, Vienna, Austria. *cir.nii.ac.jp* (2016). https://cir.nii.ac.jp/crid/1574231874043578752
81. packages, A. K. C. C. & undefined. rstatix: Pipe-friendly framework for basic statistical tests. (2019). https://cir.nii.ac.jp/crid/1360864422589421952
82. Holzapfel, G. A. & Wiley, J. Nonlinear solid mechanics: A continuum approach for engineering science. *Meccanica* **37**, 489–490 (2002).
83. Ogden, R. W. Large deformation isotropic elasticity – On the correlation of theory and experiment for incompressible rubberlike solids. *Proc. R. Soc. Lond. A Math. Phys. Sci.* **326**, 565–584 (1972).

Acknowledgements

This work was supported by the European project MAPWORMS - Mimicking Adaptation and Plasticity in WORMS Grant Agreement 101046846 (www.mapworms.eu).Micro-CT scans were also supported by BIOIMAGING-GR (MIS 5002755) implemented under "Action for Strengthening Research and Innovation Infrastructures", funded by the Operational Programme "Competitiveness, Entrepreneurship and Innovation" (NSRF 2014–2020), and co-financed by Greece and the European Union (European Regional Development Fund).

Author contributions

J.L., A.Ma., D.D., and L.M. collected the specimens and performed the biometric and the protrusion kinematics analyses. K.K. and E.V. performed the micro-CT scans and the related measurements and analyses. J.Q. and A.D.S. developed the peristaltic locomotion model. L.P., I.C., M.H.D.A., and A.Me. designed and developed the worm-inspired robotic system. L.P., J.L., I.C., M.H.D.A., J.Q., A.D.S., L.M., and A.Me. designed and developed the experimental aquaria, carried out their mechanical characterization, performed the biomechanical analyses of the worm tissues, and validated the peristaltic locomotion model. A.D.S., L.M., and A.Me. conceived the initial idea for the study and supervised the overall work. L.P. wrote the initial and final versions of the manuscript, coordinated the integration of the various contributions and revisions, and led the practical activities related to the engineering aspects of the study, while J.L. coordinated the practical activities related to the biological aspects. All authors contributed to the discussion of the results and revised the final manuscript.

Funding

This work was supported by the European project MAPWORMS - Mimicking Adaptation and Plasticity in WORMS Grant Agreement 101046846 (www.mapworms.eu).

Declarations

Competing interests

The authors declare no competing interests.

Additional information

Supplementary Information The online version contains supplementary material available at https://doi.org/10.1038/s41598-026-44047-w.

Correspondence and requests for materials should be addressed to A.M.